Human-correlated genetic HCC models identify combination therapy for precision medicine

Miryam Müller (m.mueller@beatson.gla.ac.uk)
CRUK Beatson Institute https://orcid.org/0000-0002-0751-1407

Stephanie May
Cancer Research UK Beatson Institute https://orcid.org/0000-0003-0095-7403

Holly Hall
Beatson Institute https://orcid.org/0000-0003-2779-2565

Timothy J. Kendall
University of Edinburgh https://orcid.org/0000-0002-4174-2786

Lynn McGarry
Beatson Institute for Cancer Research https://orcid.org/0000-0002-7055-2615

Lauriane Blukacz
Department of Biomedicine, University of Basel

Sandro Nuciforo
University of Basel https://orcid.org/0000-0002-1863-1869

Thomas Jamieson

Narisa Phinichkusolchit
CRUK Beatson Institute

Sandeep Dhayade
CRUK Beatson Institute

Jack Leslie
Newcastle University https://orcid.org/0000-0001-6443-2396

Joep Sprangers
CRUK Beatson Institute

Gaurav Malviya
CRUK Beatson Institute

Agata Mrowinska
Beatson Institute for Cancer Research

Emma Johnson
CRUK Beatson Institute

Misti McCain
Newcastle University https://orcid.org/0000-0002-1967-0421

John Halpin
CRUK Beatson Institute

Christos Kiourtis
CRUK Beatson Institute https://orcid.org/0000-0002-6682-5668
Anastasia Georgakopoulou
CRUK Beatson Institute
Colin Nixon
Beatson Institute for Cancer Research https://orcid.org/0000-0002-8085-2160
William Clark
Beatson Institute for Cancer Research
Robin Shaw
Beatson Institute
Ann Hedley
Cancer Research UK Beatson Institute
Thomas M. Drake
Cancer Research UK Beatson Institute
Ee Hong Tan
CRUK Beatson Institute
Matt Neilson
CRUK Beatson Institute
Daniel J. Murphy
University of Glasgow https://orcid.org/0000-0002-5538-5468
David Lewis
CRUK Beatson Institute
Helen L. Reeves
The Newcastle University Centre for Cancer, Newcastle University
Derek A. Mann
University of Newcastle https://orcid.org/0000-0003-0950-243X
Karen Blyth
Beatson Institute https://orcid.org/0000-0002-9304-439X
Markus H. Heim
University of Basel https://orcid.org/0000-0002-7523-4894
Leo M. Carlin
Cancer Research UK Beatson Institute https://orcid.org/0000-0001-7172-5234
Owen J. Sansom
Cancer Research UK Beatson Institute https://orcid.org/0000-0001-9540-3010
Crispin Miller
CRUK Beatson Institute https://orcid.org/0000-0003-4341-1283
Thomas G. Bird (✉ t.bird@beatson.gla.ac.uk)
CRUK Beatson Institute https://orcid.org/0000-0002-6120-1581

Biological Sciences - Article

Keywords:

Posted Date: May 12th, 2022

DOI: https://doi.org/10.21203/rs.3.rs-1638504/v1

Human-correlated genetic HCC models identify combination therapy for precision medicine

Authors – Miryam Müller[1,*], Stephanie May[1], Holly Hall[1], Timothy J. Kendall[2], Lynn McGarry[1], Lauriane Blukacz[3], Sandro Nuciforo[3], Thomas Jamieson[1], Narisa Phinichkusolchit[1,4], Sandeep Dhayade[1], Jack Leslie[5,6], Joep Sprangers[1], Gaurav Malviya[1], Agata Mrowinska[1], Emma Johnson[1], Misti McCain[6], John Halpin[1], Christos Kiourtis[1,4], Anastasia Georgakopoulou[1,4], Colin Nixon[1], William Clark[1], Robin Shaw[1], Ann Hedley[1], Thomas M. Drake[1,4,7], Ee Hong Tan[1], Matt Neilson[1], Daniel J Murphy[1,4], David Lewis[1,4], Helen L. Reeves[6,8,9], Derek A. Mann[5,6,10], Karen Blyth[1,4], Markus H. Heim[3], Leo M. Carlin[1,4], Owen J. Sansom[1,4], Crispin Miller[1,4], Thomas G. Bird[1,4,11,*]

Author affiliations

[1] Cancer Research UK Beatson Institute, Glasgow, UK.

[2] Centre for Inflammation Research, University of Edinburgh, Edinburgh, UK.

[3] Department of Biomedicine, University of Basel, Basel, Switzerland.

[4] Institute of Cancer Sciences, University of Glasgow, Glasgow, UK.

[5] Newcastle Fibrosis Research Group, Biosciences Institute, Faculty of Medical Sciences, Newcastle University, Newcastle upon Tyne, UK.

[6] The Newcastle University Centre for Cancer, Newcastle University, Newcastle upon Tyne, UK.

[7] Centre for Medical Informatics, Usher Institute, University of Edinburgh, Edinburgh, UK

[8] Translational and Clinical Research Institute, Faculty of Medical Sciences, Newcastle University, Newcastle upon Tyne, UK.

[9] Liver Group, Newcastle-upon-Tyne Hospitals NHS Foundation Trust, Newcastle-upon-Tyne, UK.

[10] Department of Gastroenterology and Hepatology, School of Medicine, Koç University, Istanbul, Turkey.

[11] MRC Centre for Inflammation Research, The Queen's Medical Research Institute, University of Edinburgh, UK.

* Correspondence: m.mueller@beatson.gla.ac.uk and t.bird@beatson.gla.ac.uk

Abstract

Hepatocellular carcinoma (HCC), the most common form of primary liver cancer, is a leading cause of cancer related mortality worldwide[1,2]. HCC occurs typically from a background of chronic liver disease, caused by a spectrum of predisposing conditions. Tumour development is driven by the expansion of clones that accumulated progressive driver mutations[3], with hepatocytes the most likely cell of origin[2]. However, the landscape of driver mutations in HCC is independent of the underlying aetiologies[4].

Despite an increasing range of systemic treatment options for advanced HCC outcomes remain heterogeneous and typically poor. Emerging data suggest that drug efficacies depend on disease aetiology and genetic alterations[5,6]. Exploring subtypes in preclinical models with human relevance will therefore be essential to advance precision medicine in HCC[7].

We generated over twenty-five new genetically-driven *in vivo* and *in vitro* HCC models. Our models represent multiple features of human HCC, including clonal origin, histopathological appearance, and metastasis to distant organs. We integrated transcriptomic data from the mouse models with human HCC data and identified four common human-mouse subtype clusters. The subtype clusters had distinct transcriptomic characteristics that aligned with histopathology.

In a proof-of-principle analysis, we verified response to standard of care treatment and used a linked *in vitro-in vivo* pipeline to identify a promising therapeutic candidate, cladribine, that has not been linked to HCC treatment before. Cladribine acts in a highly effective subtype-specific manner in combination with standard of care therapy.

Main text

Precision medicine for patients with advanced HCC, has lagged behind other cancers. This is not because HCC has no discernible subtypes, but because targeting these has proved challenging. Tyrosine kinase inhibitors (TKIs: e.g. sorafenib[8] and lenvatinib[9]) were the only first-line treatments for unresectable HCC until 2020. Thereafter, the IMbrave150 study (atezolizumab with bevacizumab)[10] highlighted the potential of combination approaches with immune checkpoint inhibition (ICI) therapy, with enhanced responses for some patients and improved overall survival. Alongside advances in treatment options came an increased appreciation that heterogeneous treatment responses in HCC patients provide a potential for patient stratification[5,6]. The lack of necessity for clinical biopsies in advanced HCC has resulted in a lack of tissue from late-stage disease. This hinders advances in defining clinically relevant stratification biomarkers and mechanistic understanding within subtypes for these patients. Preclinical models offer a biological platform for disease interrogation, but currently, few

models faithfully recapitulate the complexity of human disease or have been validated against transcriptomic and phenotypic human HCC profiles[11,12]. Thus, there is currently a need for human-relevant preclinical models, to investigate therapy efficacies, providing guidance on subtype-specific treatments for different patient populations.

Development and characterization of a suite of genetically-driven murine HCC models

To address this need, we first set out to generate a broad range of mouse models guided by the most commonly found genetic drivers of human HCC[4]. Human HCC is thought to evolve from a hepatocytic clonal origin[3,13]. We reproduced this aspect of cancer biology in our models by introducing the genetic alterations into adult murine hepatocytes using conditional recombination technology and allowing the premalignant clones to evolve to HCC over time.
We intravenously injected adult mice with a viral vector encoding Cre recombinase with a hepatocyte tropism due to its thyroxine-binding Globulin (TBG) promoter, AAV8-TBG-Cre. This drove clonal recombination of endogenous floxed alleles in individual hepatocytes in an immune-competent environment (**Fig. 1a**). AAV8 was titrated to a dose (6.4*10^8 genomic copies (GC)/mouse) that resulted in clonal targeting and was highly hepatocyte-specific (**Extended Data Fig. 1a-d**). Recombination occurred primarily in the first five days after injection, was observed across all three hepatocyte zones[14], but was significantly different between male and female mice (**Extended Data Fig. 1e-h**). This led to a lower tumour count and consequently extended survival in females after induction of HCC-related oncogenes (**Extended Data Fig. 1i-k**). Furthermore, varying induction dose or mutational burden affected tumour occurrence and speed of progression to endpoint (**Extended Data Fig. 1i+l**).
Next, we applied this strategy to a broad range of HCC relevant oncogene/tumour suppressor combinations using a standardized dose in male mice unless otherwise stated. We particularly focused on genes identified by a TCGA study[4] belonging to the WNT pathway, the cell cycle, or the RTK/RAS/PI3K pathway growth (**Fig. 1b**). We decreased the AAV induction titre in specific instances (Cohorts 14, 15, 23, and 24: 1.28*10^8 GC/mouse) to reduce the clonal burden, facilitating progression of these more aggressive models to larger individual tumours. We monitored thirty-five genetically distinct models, including models with a whole-body knockout of *Cdkn1a* or *Cdkn2a*, for liver nodule growth for minimum 230 days following induction (**Extended Data Fig. 1l, Extended Data Fig. 2a**).
The majority of our models (83%) developed end-stage tumours within the study timeframe and most (69%) showed a tumour penetrance of higher than 50%. Surprisingly, some

combinations, e.g. *MYC* overexpression + *Trp53* alteration, which induced HCC in previously published models[12], had very low to no tumour penetrance using our clonal evolution approach and did not reach end-stage tumours within the observed period. Reflective of human disease we observed intra-tumoural haemorrhaging and/or rupture (bleeding) as well as metastatic spread to the lung, one of the main metastatic sites in human HCC together with bone and lymph nodes[2,15] (**Fig. 1b-d, Extended Data Table 1**). We observed a negative correlation between an increased amount of driver mutations and survival, in spite of reduced clonal induction with a lower AAV titre, and a positive correlation between an increased amount of driver mutations and tumour proliferation, as well as between mutational burden and lung metastasis in our cohorts (**Extended Data Fig. 2b**). Tumour haemorrhage did not correlate significantly with mutational burden but occurred predominantly in cohorts with an "activated *Ctnnb1* and *Pten* loss without *MYC* overexpression" mutational pattern (**Extended Data Fig. 2c**). Macroscopic and microscopic appearances were consistent with human HCC and covered a wide range of histological phenotypes. This included well-differentiated HCC (e.g. Cohorts 5 + 19), undifferentiated HCC (e.g. Cohorts 23 + 28), pseudoglandular HCC (e.g. Cohort 30) and steatotic HCC (e.g. Cohort 35) (**Fig. 1c, Extended Data Fig. 3**). Lung metastatic lesions reflected primary tumour histopathology (**Fig. 1d**). Histopathological assessment of morphological parameters is currently the gold standard for differential diagnosis of liver cancer in patients[16]. They showed strong similarities to human HCC histopathology, including typically observed architectural patterns (trabecular, glandular, solid, and nested) and cytological atypia. Different combinations of genetic alterations resulted in distinct morphologies (**Fig. 1e**).

In summary, we used combinatorial genetic alterations, relevant to human HCC, to drive the development of autochthonous tumours in twenty-seven immunocompetent mouse models. Tumour growth happened progressively over several months with individual hepatocytes as the cell of origin. These models recreate key features characteristic of human HCC biology, including histopathological phenotypes and metastatic spread.

Transcriptional alignment classifies four common human/mouse (HuMo) clusters with distinct features.

To determine how well our models further represent human HCC we performed unbiased transcriptional analysis. We included a range of well-established carcinogen-induced (TOX)

and transplant (OT) HCC mouse models with our genetically engineered mouse models (GEMMs) to make this comparison more comprehensive (**Fig. 2a**).

Using nonlinear dimensionality reduction (Uniform Manifold Approximation and Projection, UMAP[17]) we mapped mouse end-stage HCC data onto the human HCC data[4] (**Fig. 2b)**. Individual models, both genetically modified and non-genetically modified, clustered within different regions in the UMAP plot (**Extended Data Fig. 4a)**. Mutational status, however, is not always indicative of signalling status[18] and genomic profiling of human HCC previously showed that mutations are not exclusively prognostic of association with specific subtypes[4]. This is especially relevant for advanced disease stages with a relatively high mutational burden[19], where different genetic alterations can influence each other. We show that e.g. mutations in *CTNNB1/Ctnnb1* do not always lead to upregulation of expression of downstream pathway targets (*GLUL/Glul*, *LGR5/Lgr5*, *LECT2/Lect2*, or *NOTUM/Notum*) in either species **(Extended Data Fig. 4b-f)**. Our murine data also supports the observation that mutational status by itself is not always predictive of the resemblance between cohorts (**Extended Data Fig. 4a**).

We therefore went on to compare the human and mouse transcriptome data based on functionally and mechanistically relevant pathway enrichment. We used the Louvain method for community detection[20] to identify groups in our human/mouse HCC data set (**Fig. 2c**). We detected four major human/mouse (HuMo) clusters (**Fig. 2d**). Genetic mouse models are represented in all four clusters with varying heterogeneity within cohorts, whereas the purely carcinogen-induced models are only representative of HuMo cluster 2 (**Fig. 2e**). Pathway enrichment analysis could establish cluster-specific characteristics. HuMo cluster 1 was enriched for pathways linked to metabolism and differentiation, but had negative enrichment for proliferation and inflammatory pathways. HuMo cluster 2 was related to cluster 1 but was distinct particularly through a higher enrichment in pro-inflammatory pathways. HuMo clusters 3 and 4 were both poorly differentiated and highly proliferative, with cluster 4 showing enrichment in epithelial-to-mesenchymal transition (**Fig. 3a**).

To assess if the transcriptional clustering corresponded to similar histopathological features in mice and human HCC within the same cluster we compared our mouse tumours to TCGA tissue[4]. We observed that mouse and human tissue belonging to the same HuMo cluster did indeed have analogous morphological characteristics (**Fig. 3b**). Tissue from HuMo cluster 1 showed well-differentiated HCC. HuMo cluster 2 tissue presented with steatosis and immune cell infiltration. HuMo clusters 3 and 4 tissue displayed deposition of extracellular matrix and moderately (cluster 3) to poorly (cluster 4) differentiated HCC (**Fig. 3b**).

Our clustering is better suited than previously established and clinically used subgroups of human HCC, such as the Hoshida classification[21], for comparing mouse and human data and identifying common subgroups (**Extended Data Fig. 5a**). It also surpasses previous attempts of comparing mouse and human HCC data in scale and detail[11,12]. Our clustering approach distinguished two patient populations within Hoshida subclass S3, namely HuMo clusters 1 and 2 (**Fig. 2d, Extended Data Fig. 5a+b**). Hoshida *et al.* implied that S3 might consist of two subpopulations with *CTNNB1* as a dividing factor, but did not use this as a factor in their classification[21]. This distinction in our analysis resulted in differences in patient survival, unappreciated when using the Hoshida classification, with patients associated with HuMo cluster 2 having had an improved survival probability relative to patients associated with the other HuMo clusters. (**Extended Data Fig. 5c+d**). Additionally, we observed corresponding survival probabilities in the related GEMMs when plotting survival of all GEMM mice based on their HuMo cluster association, with the longest survival in HuMo cluster 2 mice and the shortest in HuMo cluster 4 mice (**Extended Data Fig. 5e**).

In brief, we identified four distinct clusters, common across human and mouse models, by integrating our mouse transcriptional data with human HCC transcriptional data. Our models recapitulate transcriptionally the full range of human HCC, including within individual clusters. What is more, this aligned with similar histopathological features and relative survival within clusters, with specific GEMMs representative of individual subtypes of human HCC.

Tyrosine kinase inhibition but not immune checkpoint inhibition increased survival in a representative cohort of HuMo cluster 1.

To explore the translational potential of our models, we investigated response to standard of care treatments. We focused on one model in a proof-of-principle set of experiments. Approximately 30% of HCC patients have mutations leading to activation of the beta-catenin signalling pathway[4]. HCC with activated beta-catenin signalling has a low enrichment score for immune signatures and has been, in most cases, associated with immune exclusion[22,23]. Furthermore, active beta-catenin pathway signalling has been linked to ICI resistance in a prospective HCC cohort study[5], suggesting a need for alternative treatment options for this patient subgroup. In the TCGA data set 64% (56/88) of patients with mutations in *CTNNB1* were associated with HuMo 1 and made up 47% (56/118) of patients in that cluster (**Extended Data Fig. 6a+b**). Additionally, humans and mice associated with HuMo cluster 1 had immune-cell paucity and a low immune-score (**Extended Data Fig. 6c+d**). We, therefore, identified

HuMo cluster 1 as the one most likely to correspond to the group of patients with activated beta-catenin pathway signalling that would benefit from alternative treatment options. Cohort 5 (*Ctnnb1*$^{ex3/wt}$ + R26$^{LSL\text{-}MYC/LSL\text{-}MYC}$, from here on referred to as BM) mice were used as a representative model and showed phenotypic resemblance to human *CTNNB1*-mutated HCC (**Extended Data Fig. 6e**).

We aimed to mimic the treatment of established tumour lesions. Therefore, we first performed a time-course analysis for tumour onset in the BM mouse model (Cohort 5) to determine an appropriate time point for the start of treatment. We observed clonal induction of hepatocytes, which evolved over time into microscopic lesions and then macroscopic tumour nodules, with GS as a marker of beta-catenin driven tumour induction (**Fig. 4a-c**). Tumour evolution from single clones led to moderate inter-tumoural and inter-murine transcriptional heterogeneity in end-stage tumours, including activation of pro-tumorigenic pathways such as proliferation or angiogenesis. However, while gene expression in tumours was strikingly different to non-tumour tissue, it was also consistently different to livers with a global hepatocytic short-term expression of the same oncogenes (**Extended Data Fig. 7a-d**). This implied a consistent trajectory of clonal evolution occurring during tumour progression[3,13]. Relevant long-term models where this evolution can take place are essential for studying HCC in preclinical models.

We started drug treatment at d90, based on 100% of Cohort 5 (BM) mice having macroscopic tumours and 96% of Cohort 5 (BM) mice surviving past this time point (**Extended Data Fig. 2a, Fig. 4a-d**). Cohort 5 mice showed a significant increase in survival upon treatment with the TKIs, sorafenib and lenvatinib (**Fig4. e+f**). However, treatment with the ICI agent anti-PD1 did not impact overall survival in this cohort (**Fig. 4g**). These results are similar to the reported drug responses to TKIs and ICI in human patients with activated beta-catenin signalling[5]. In contrast, ICI has been used successfully in orthotopic and carcinogen-induced mouse models as reported by Leslie *et al* [24].

We observed changes in macroscopic and microscopic appearances in end-stage tumours of Cohort 5 (BM) mice treated with lenvatinib. Tumours were different in colour and stiffer. Microscopic HCC patterns shifted from mostly well-differentiated to a poorer differentiated phenotype with greater stromal presence (**Extended Data Fig. 8a-c**). Furthermore, more mice in this treatment arm presented with lung metastases compared to vehicle treatment or other treatments (**Extended Data Fig. 8d**). Monitoring of tumour growth via magnetic resonance imaging suggested a delayed and decreased tumour growth initially upon lenvatinib treatment (**Extended Data Fig. 8e**). We also observed a higher metastatic burden in a second model

(Cohort 23, BM + *Pten*$^{fl/fl}$ + *Trp53*$^{R172H/wt}$ + *Cdkn2a*$^{KO/KO}$) with increased survival after lenvatinib treatment (**Extended Data Fig. 8f-h**). We hypothesized that the increased aggressiveness, manifested by morphological changes and greater metastatic burden, resulted from the extended survival coupled with an altered phenotype associated with acquired resistance to lenvatinib therapy. We, therefore, investigated livers of Cohort 5 (BM) mice after 15 days and 30 days of lenvatinib treatment from day 90 post induction (**Fig. 4d**). We observed no differences in tumour morphology, but a decreased tumour burden through less proliferation but without increased cell death, at both 15 and 30 day time points in lenvatinib treated mice (**Fig. 4h-j**). There were no detectable metastases at either time point, supporting our hypothesis that the heightened aggressiveness in this model is a late-stage on-treatment event.

Overall, treatment responses in this specific GEMM, were reminiscent of a distinct, common, and difficult to treat subtype of HCC, characterised by a transient survival benefit observed in human phase 3 clinical studies[8,9].

A high-throughput tumoroid assay pipeline identified anti-cancer drugs for repurposing as potential HCC therapy in a subtype-specific manner.

After establishing the response to current standard of care treatments of mice representative of HuMo cluster 1 (Cohort 5, BM), we concentrated on identifying novel therapeutic options for this difficult-to-treat subgroup. We performed an *in vitro* high-throughput screen, based on GEMM-derived HCC organoids (HCCOs)[25], with subsequent *in vivo* validation in the respective GEMM (**Extended Data Fig. 9a**).

HCCOs recapitulate the transcriptomic profile, histological organization, and tumorigenic potential of the primary tumour[26,27] and are therefore suited to investigate drug effects on tumour cells. They allow for rapid testing of a large range of drugs and for a side-by-side comparison between mouse-derived and human-derived tumour cells.

HCCOs derived from end-stage tumours of Cohort 5 (BM) mice expressed beta-catenin and downstream target glutamine synthetase, as well as markers of proliferation (Ki67) and differentiation (HNF4a), features shared with the corresponding primary tumour (**Extended Data Fig. 9b**). We tested a comprehensive drug library consisting of the 147 FDA-approved anti-cancer drugs available at the time (June 2019) plus internal controls and analysed their effect on HCCO growth (**Fig. 5a, Extended Data Table 2**). The most efficacious drugs were a group of antimetabolites: nucleobase analogues that interfere with DNA synthesis (**Fig. 5a, Extended Data Fig. 9c**). We validated the dose-dependent effect of cladribine, the most

effective antimetabolite, both in several distinct mouse and human HCCOs. This confirmed the results of the screen and demonstrated the nanomolar potency of cladribine (**Fig. 5b+c**). We also tested selected other drugs from our screen. Lenvatinib and sorafenib, which are understood to act principally upon the tumour microenvironment, showed little tumour-epithelial efficacy in both the screen and separate validation (**Extended Data Fig. 9d-f**). Next, we treated Cohort 5 (BM) mice, representing HuMo cluster 1, with either cladribine monotherapy or combination therapy of cladribine and lenvatinib, as a standard of care TKI (**Fig. 6a+b**). Cladribine monotherapy led to increased survival but combination therapy extended survival further (**Fig. 6c**). Cladribine monotherapy reduced the number of tumours, but the remaining tumours still progressed to end-stage HCC. Combination therapy with lenvatinib showed synergistic effect, almost completely eradicating all tumours (**Fig. 6d+e**). Study progression to either clinical tumour endpoint or study endpoint (d270 post induction) was limited in some animals (31% cladribine, 62% cladribine + lenvatinib) due to clinically significant weight loss (< 80%).

Treatment with either monotherapy or combination therapy showed a decrease in proliferation in end-stage tumours, but no alteration in apoptotic cell death. Interestingly, we observed an increase in $CD3^+$ T-cell infiltration into the tumour after combination therapy compared to vehicle (**Extended Data Fig. 10a-d**). Since time of endpoint varied greatly between the different treatments, we analysed tumours at a defined time point of 30 days post treatment start. Mice on monotherapy or combination therapy showed decreased tumour size and number, with a significant decrease in proliferation (**Fig. 6f+g, Extended Data Fig. 10b+e**). Both healthy and tumour tissue exhibited a greater extent of DNA damage (pH2AX), as expected after treatment with a nucleobase analogue, but this did not alter upregulation of another senescence marker (p53) nor apoptosis (**Extended Data Fig. 10f-h**). Again, we observed increased infiltration of $CD3^+$ T-cell into the tumour of mice treated with combination therapy (**Fig. 6h**). Finally, we tested whether cladribine, either as monotherapy or in combination with lenvatinib, is equally effective in mouse models representing other HuMo clusters. We treated Cohort 23 (BM + $Pten^{fl/fl}$ + $Trp53^{R172H/wt}$ + $Cdkn2a^{KO/KO}$) mice, representing HuMo cluster 4, and Cohort 43 ($R26^{LSL\text{-}MYC/LSL\text{-}MYC}$ + $Kras^{G12D/wt}$) mice (induced with a higher titre of AAV-TBG-Cre than Cohort 32 to increase tumour burden to make survival time comparable to Cohort 5), representing HuMo cluster 2 (**Fig 6b**). Both monotherapy and combination therapy were effective in prolonging the survival of Cohort 23 mice (**Fig. 6i**). However, cladribine failed to extend the survival in Cohort 43 mice, a wild-type *Ctnnb1* model with mutated *Kras*, either as monotherapy in combination therapy with lenvatinib (**Fig. 6j**).

In a proof of concept, we demonstrated the potential of our GEMM platform to identify epithelial targeting therapies which synergised effectively with the standard of care treatments, the latter of which mainly targeting the tumour microenvironment. This novel combination of TKI and repurposed FDA-approved anti-cancer compound led to highly effective subtype-specific treatment responses.

Discussion

We used a range of genetic alteration frequently associated with human HCC[4] to develop a suite of immunocompetent mouse models that closely resembles the development and progression of human HCC with hepatocytes as the cell of origin. Overall, our models successfully recreate different key molecular and pathophysiological events typical of human HCC, including tumour haemorrhaging and metastases to the lung[2,15]. Furthermore, they mimic various tumour microenvironments such as immune active and immune desert tumours or high stroma and low stroma tumours. We demonstrated clinical relevance of our models by integrating mouse data with a publically available human HCC data set, defining shared subtypes, and proving response to standard of care treatment. Furthermore, we showed these models can be used as a preclinical platform, together with HCCOs, for investigating rapid drug repurposing, but also in further studies to study tumour evolution and mechanisms as well as drug resistance.

We appreciate, that not all genetic alterations associated with HCC have been tested in this study. *TERT* promoter modifications, despite being very frequent in human HCC (up to 60% of patients)[19], are difficult to model appropriately in mice due to biological differences between species. Mice have very long telomeres and it would take several generations of crossing mice with *Tert* deletions before detecting a noticeable effect of re-activating *Tert*[28]. In our opinion that is an obstacle that will be difficult to overcome in mouse models of HCC and other means are needed to study *TERT* promoter mutations and their therapeutic targetability. However, since *TERT* promoter mutations are so omnipresent in HCC, they might be less relevant for subtyping and we did not discover a specific human *TERT* group that was separate from our GEMMs.

Furthermore, some combinations of genetic alterations showed low to no tumour penetrance in our GEMMs, e.g. *Trp53* modifications in combination with *MYC* overexpression, while these showed high penetrance in HCC in previous models using hydrodynamic tail vein injections[12]. Administration of hydrodynamic tail vein injection has been shown to cause apoptosis in the

liver[29], leading to higher inflammation and favourable conditions for tumour development. Additionally, levels of MYC might be a determining factor in a clone progressing to a tumour[30]. Whilst the majority of our studies was performed in male mice, we found no indication that the results are sex-specific. Indeed, when we used the same genetic alterations in female mice we observed a similar phenotype and cluster association (Cohort 5, BM, male vs. Cohort 6, BM, female). However, AAV-TBG-Cre induction seems to be less potent in female mice, which is particularly prominent in models with a lower mutational burden. Future experiments are needed to include genetic alterations or risk factors predominantly associated with female HCC in patient stratification, such as *Bap1* mutations or malignant transformation of hepatocellular adenomas[4,31].

Beyond the investigation of further genetic alterations, our models can also be easily combined with environmental liver disease models, such as high-fat diets. Preliminary data from our transcriptomic analyses indicated that genetics dominate cluster association, with the addition of background fibrotic disease having little transcriptomic influence (Cohort 5 vs 37). However, future research incorporating multifaceted environmental factors is needed to better understand HCC biology in human patients who usually present with chronic liver disease and hepatic impairments, which impact the treatment strategy available to them[2,16].

Our models strike a balance between allowing time for tumour evolution while still being time-efficient. This enables future detailed investigation of tumour evolution and factors contributing to malignant transformation, especially as not all of the recombined clones expand into tumours.

Somatic mutations are poorly clinically actionable in HCC and remain difficult to target therapeutically. In the case of multiple genetic alterations, each individual contribution to tumorigenesis might be difficult to determine[32–34]. Our models with their increased complexity of multiple genetic alterations, similar to the mutational burden of late stage HCC[19], allow for the exploration of alternative targets and might contribute to understanding mutational dominance in different contexts. Additionally, by mimicking clonal evolution, they might help to identify the stage in tumour development – initiation, early nodule growth, malignant transformation - when a drug has an optimal effect.

We show that HCCOs are a tractable and rapid platform to identify treatments in combination with efficacy testing *in vivo*, and promote the principles of the 3Rs (Replacement, Reduction and Refinement) for humane animal research. However, current cell culture conditions limit the translatability of HCCO-based drug response predictions and, therefore, validation in animal models remains essential. Future research in HCCOs needs to overcome the reduced

complexity in cell culture, a general issue in organoid culture[35], and address options for co-culture with cells shaping the tumour microenvironment[36]. Modifying HCCOs with CRISPR technology may also provide useful insights to explore tumour biology and mechanisms beyond drug vulnerabilities[37].

Most importantly, we show that our GEMMs map transcriptionally and histologically to human HCC. Using a computational biology approach has enabled us to not only position our GEMMs and select carcinogen-induced models against human HCC, but to furthermore identify four shared subclasses with defining characteristics. Interestingly, some of our models show a degree of heterogeneity often observed in human HCC[38], with tumours associated to several HuMo clusters. Our newly developed GEMMs represent all identified subtypes, whereas chemical carcinogen-induced models included in this study only mapped to one HuMo cluster (cluster 2).

Our preclinical platform and classification system can be used as a resource for the HCC research community to streamline preclinical research and increase comparability of different mouse models. Furthermore, linking preclinical models with patient data can aid in stratifying patients to treatment, identifying novel therapies, and improving the likelihood of translational success. The HCCO screen allowed us to rapidly identify and test an FDA-approved anti-cancer drug, cladribine - not previously linked to HCC, in a clinically relevant model. We could show efficacy and improved survival *in vivo* together with standard of care treatment, which will allow for a swift translation into the clinic.

We believe that our approach of linking preclinical models to human data in a subtype-specific manner will also be applicable, cross-referable, and advantageous in translational research of other solid cancers.

Abbreviations:

Ctnnb1$^{ex3/wt}$ + R26$^{LSL\text{-}MYC/LSL\text{-}MYC}$ (BM), Genetically engineered mouse models (GEMMs), Genomic copies (GC), Hepatocellular carcinoma (HCC), Hepatocellular carcinoma organoids (HCCOs), Human/Mouse (HuMo), Immune checkpoint inhibition (ICI), Tyrosine kinase inhibitors (TKIs), Uniform Manifold Approximation and Projection (UMAP)

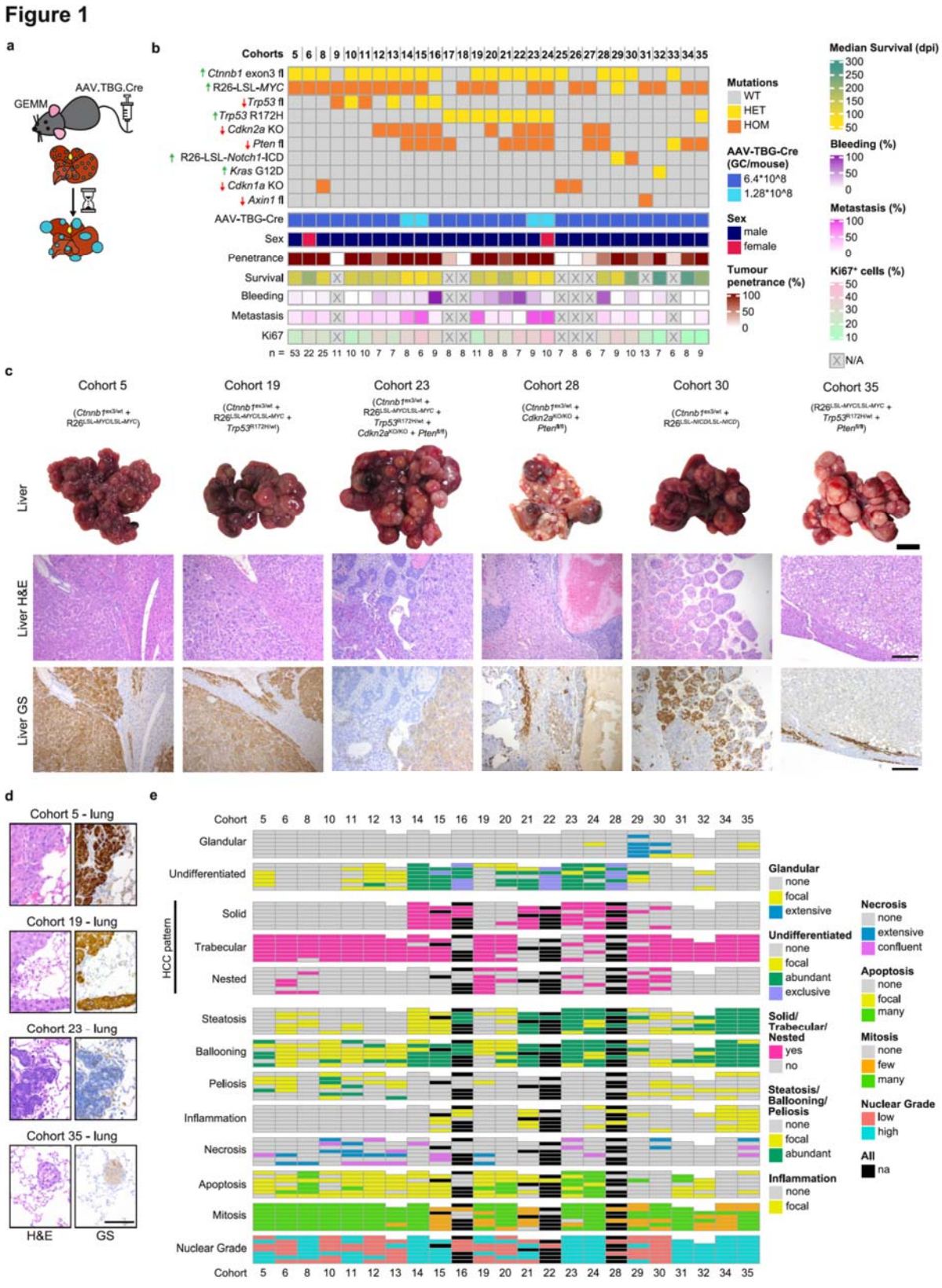

Figure 1: Comprehensive characterization of novel genetic HCC mouse models. (a) Experimental scheme. Conditional genetically-engineered mice induced with AAV-TBG-Cre virus develop tumours after clonal recombination of genes classically associated with HCC in

403 a TCGA study[4]. **(b)** Specific combinations of mutations, but not amount of mutations, drive
404 model-specific features such as survival, tumour proliferation (Ki67), bleeding from tumour,
405 and metastasis in murine models of HCC. Arrows represent gain-of-function (green) or loss-
406 of-function (red). For exact values see **Extended Data Table 1**. **(c)** Representative images
407 show variation of macroscopic and microscopic phenotype depends on combinations of
408 mutations. Glutamine synthetase (GS) serves as indicator of activated CTNNB1 signalling.
409 Scale bar equals 1cm (macroscopic) or 200µm (microscopic). Full range of GEMMs shown in
410 **Extended Data Fig. 3**. **(d)** Representative images show lung metastases resembling primary
411 tumour phenotype as demonstrated by H&E and glutamine synthetase (GS) staining. Scale bar
412 equals 100µm. **(e)** Murine HCC models present common patterns and characteristics used for
413 identification and classification of human HCC based on in-depth histopathological
414 examination. n = 5-7 mice per cohort as indicated by bars.

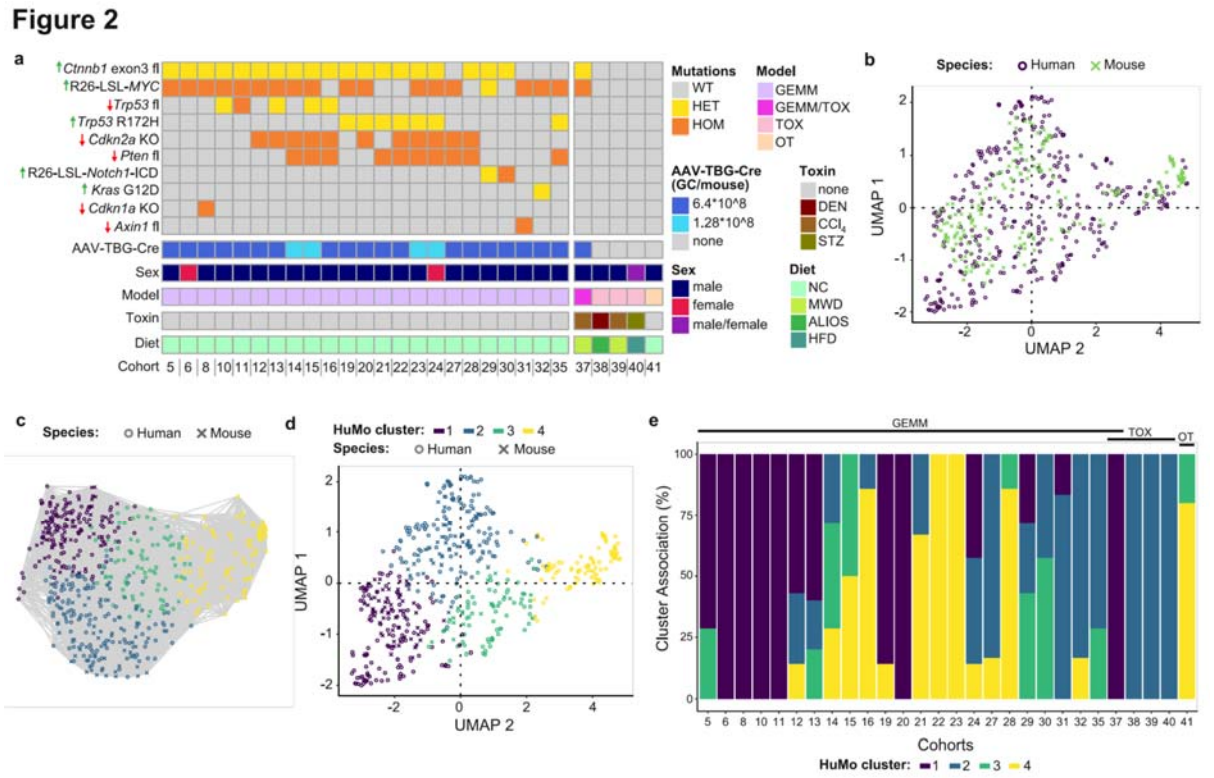

Figure 2: Transcriptional alignment classifies 4 common human/mouse (HuMo) clusters. **(a)** Summary overview of murine models used for transcriptional analysis. In addition to the genetically-engineered mouse models (GEMMs), described in **Fig. 1**, carcinogen-induced (TOX) and orthotopic transplant (OT) models were included. These include mice treated with diethylnitrosamine (DEN), carbon tetrachloride (CCl_4), and streptozotocin (STZ), as well as multiple diets: modified western diet (MWD), American lifestyle-induced obesity syndrome (ALIOS), high-fat diet (HFD), or normal chow (NC). **(b)** UMAP visualisation demonstrates overlap of mouse (GEMM, TOX, and OT) and the TCGA human HCC transcriptional data set. **(c)** Unbiased clustering using a Louvain community detection algorithm identifies four groups within human and mouse (GEMM, TOX, and OT) HCC data. **(d)** Distribution of subgroups identified in **(c)** with UMAP highlights shared human/mouse (HuMo) clusters. **(e)** All HuMo clusters are represented in the analysed GEMMs with varying heterogeneity within the individual cohorts. GEMM = genetically engineered mouse model, TOX = carcinogen-induced model, OT = orthotopic transplant model.

Figure 3

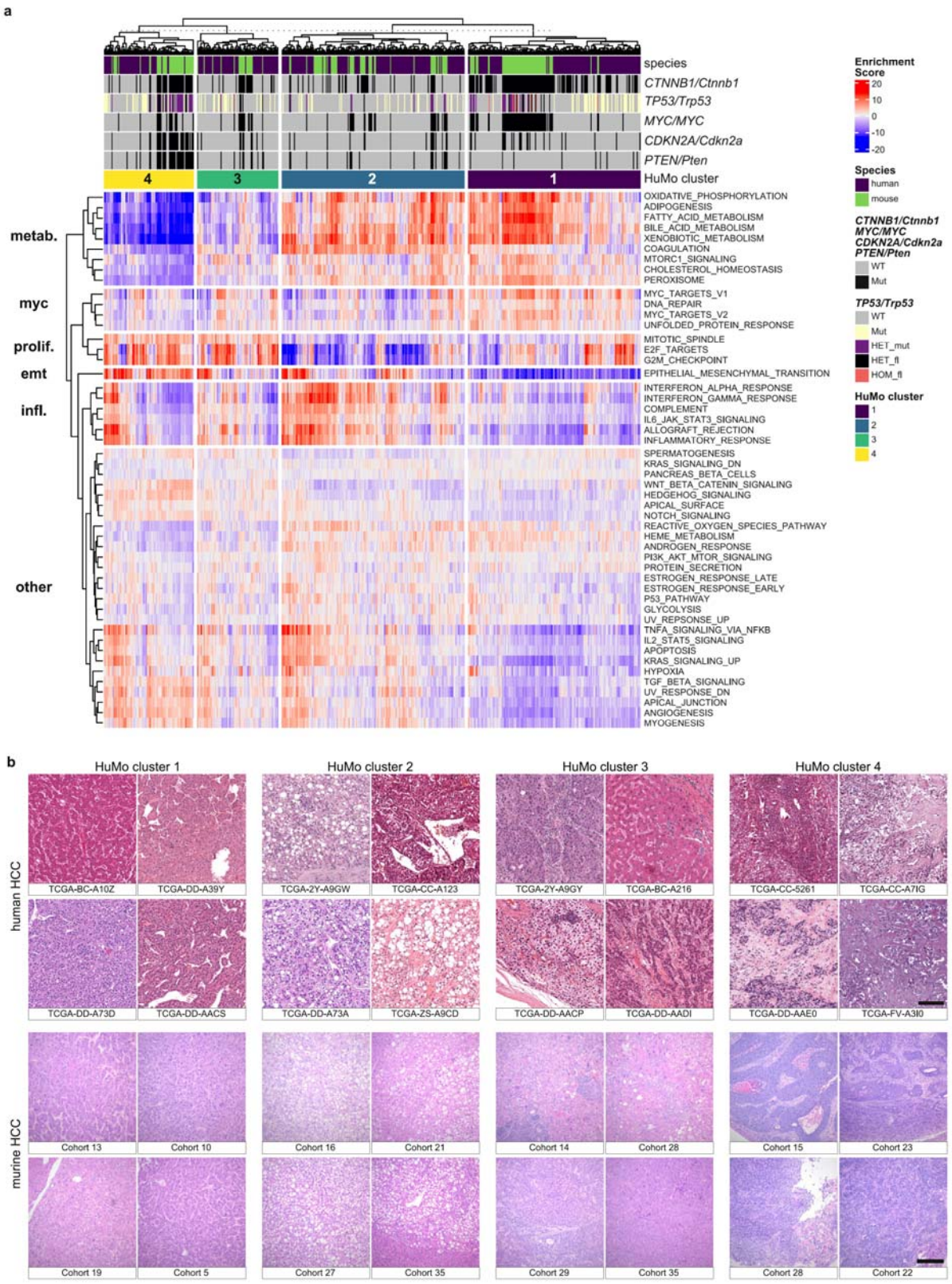

Figure 3: Individual HuMo clusters have distinct transcriptional and histological features. (a) Heatmap of pathway enrichment analysis across the GEMMs, non-GEMMs and human TCGA-HCC data[4] indicates distinct identifying characteristics, including metabolic

activity/differentiation (metab), *MYC/Myc* pathway activation (myc), proliferation propensity (prolif.), epithelial-to-mesenchymal transition (emt), or inflammatory status (infl.), for the four HuMo clusters. n = 371 (human) and 187 (mouse). **(b)** Transcriptional alignment correlates with histopathological similarities between human and mouse liver samples from the same HuMo clusters as shown by H&E staining. Scale bars equal 200µm.

Figure 4

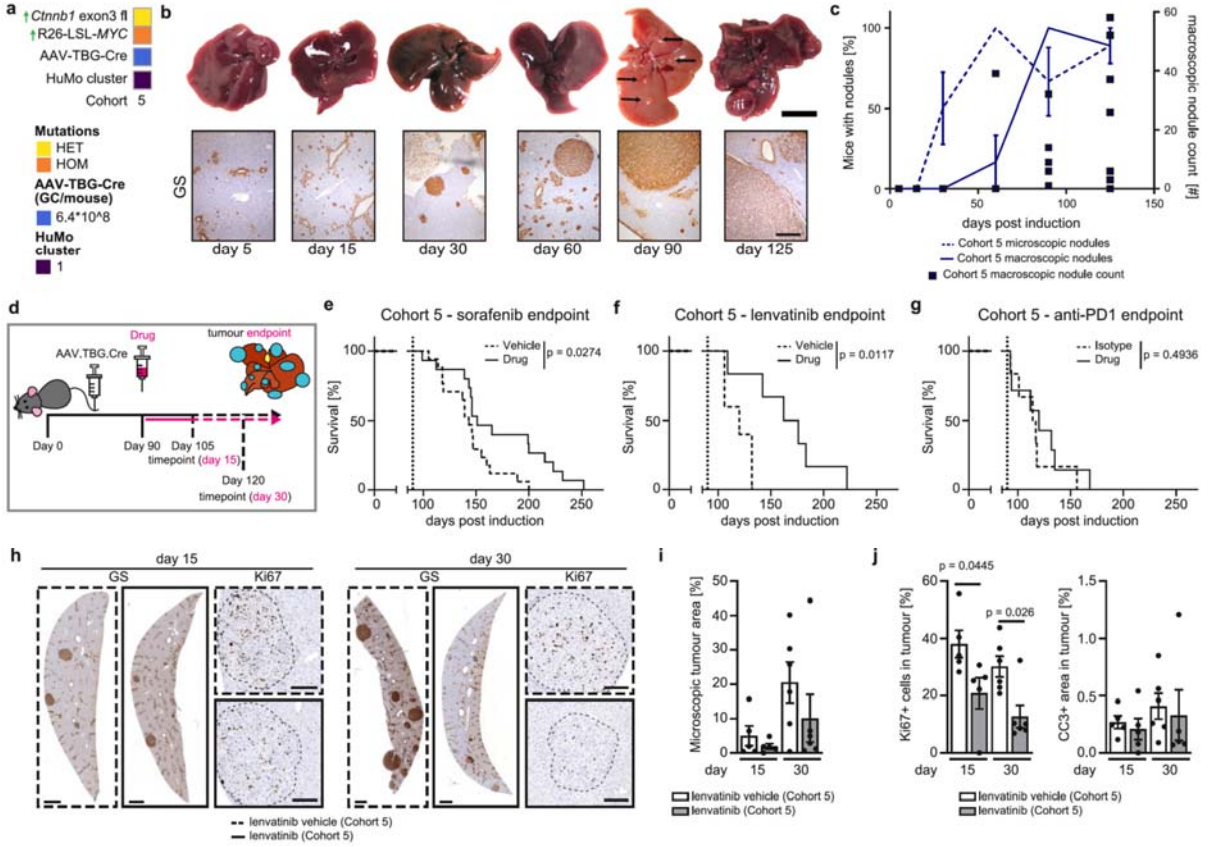

Figure 4: Tyrosine kinase inhibition, but not immune checkpoint inhibition leads to decreased tumour growth and increased survival in a representative mouse cohort of HuMo cluster 1. (a) Summary of cohorts used in **b-j. (b)** Temporal tracking of tumour development from single clone to established HCC in Cohort 5 (BM, male) mice. Tracking of early clones and microscopic nodules via glutamine synthetase (GS). Tracking of late nodules via macroscopic whole liver assessment. Black arrows indicate macroscopic lesions at d90. Scale bars equal 200µm (microscopic images) and 1cm (macroscopic images). **(c)** Quantification of microscopic nodule presence, macroscopic nodule presence and macroscopic nodule count over time in Cohort 5 (BM, male) mice. n = 5 (d15), 6 (d5, d30, d60, d90), 9 (d125). Data shown as mean ± s.e.m. (microscopic and macroscopic nodules, %) or individual data (nodule count, #). **(d)** Treatment scheme for **e-j** with drug given from d90 post induction. **(e+f)** Treatment with tyrosine kinase inhibitors sorafenib (45mg/kg, oral) **(e)** or lenvatinib (10mg/kg, oral) **(f)** significantly increases survival in a mouse model representative of HuMo cluster 1 (Cohort 5: BM, male). Dotted vertical line indicates treatment start. n = 17 (sorafenib vehicle), 15 (sorafenib), 5 (lenvatinib vehicle), 6 (lenvatinib). Log rank test. **(g)** Treatment with immune checkpoint inhibitor anti-PD1 (200µg/mouse, ip) does not affect survival in a mouse model representative of HuMo cluster 1. Dotted vertical line indicates treatment start. n = 6

(IgG Isotype), 7 (anti-PD1). Log rank test. **(h-j)** Time point analysis, day 15 and day 30 post drug, of lenvatinib treated mice show a reduction in total number of liver lesions, and a significant reduction of proliferation, assessed by Ki67+ cells, in the lesions, but no increase of apoptotic cell death through cleaved Caspase 3 (CC3) and no change of tumour morphology. **(h)** Representative images of glutamine synthetase (GS) and Ki67 staining in lenvatinib and vehicle treated mice at day 15 and day 30. Dotted line indicates tumour border. Scale bar equals 1mm (GS) or 200µm (Ki67) **(i)** Quantification of microscopic tumour area (independent of GS status). n = 5 (day 15 vehicle + lenvatinib), 6 (day 30 vehicle + lenvatinib). Data shown as mean ± s.e.m. Unpaired t-test (day 15)/Mann-Whitney test (day 30). **(j)** Quantification of $Ki67^+$ and $CC3^+$ tumour area. n = 5 (day 15 vehicle + lenvatinib), 6 (day 30 vehicle + lenvatinib). Data shown as mean ± s.e.m. Unpaired t-test (day 15)/Mann-Whitney test (day 30).

Figure 5

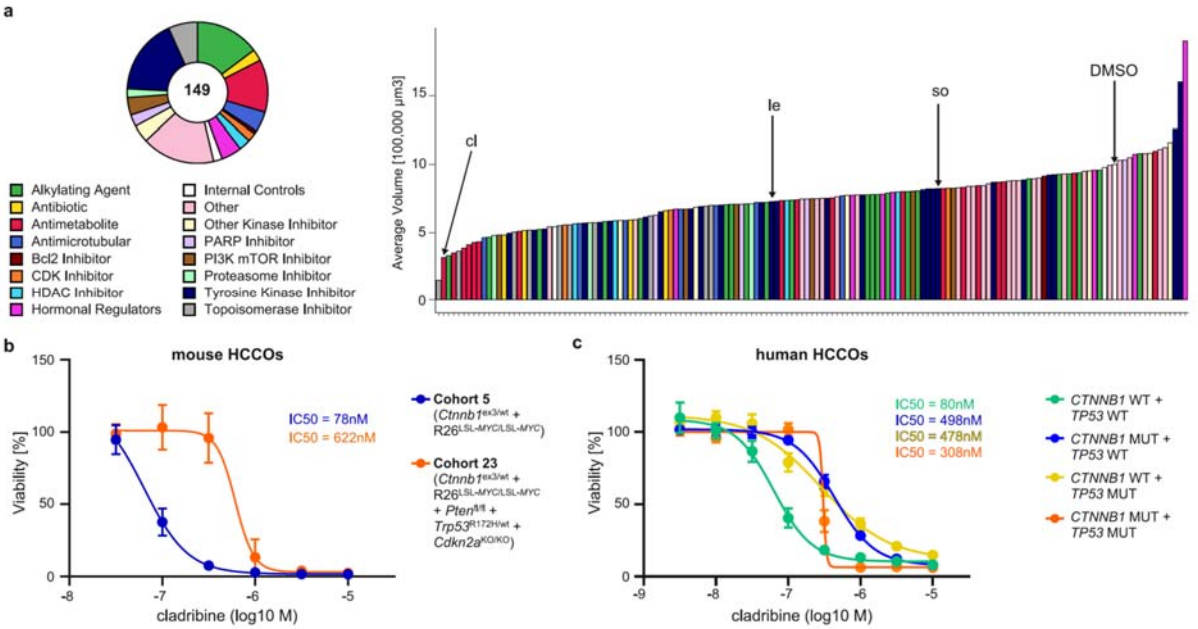

Figure 5: A high-throughput HCCO assay pipeline identifies purine analogues such as cladribine as a novel class of therapeutics for HCC treatment. (a) High-throughput screening of a panel of 147 FDA-approved anti-cancer drugs plus internal controls highlights antimetabolites having an effect on growth of tumoroids from Cohort 5 (BM, male) mice, with cladribine (cl) having the greatest effect. Both lenvatinib (le) and sorafenib (so) only have a mild effect on the tumour cells directly. For a detailed ranking, see **Extended Data Table 2**. **(b+c)** *In vitro* validation of cladribine efficacy demonstrates a dose-dependent effect on both murine **(b)** and human **(c)** HCCOs. n = 3 (different passages from one HCCO line per named mouse cohort, technical duplicates), 3 (different passages from one to ten human HCCO lines per driver combination, see methods for details, technical duplicates). Data shown as mean ± s.e.m.

Figure 6

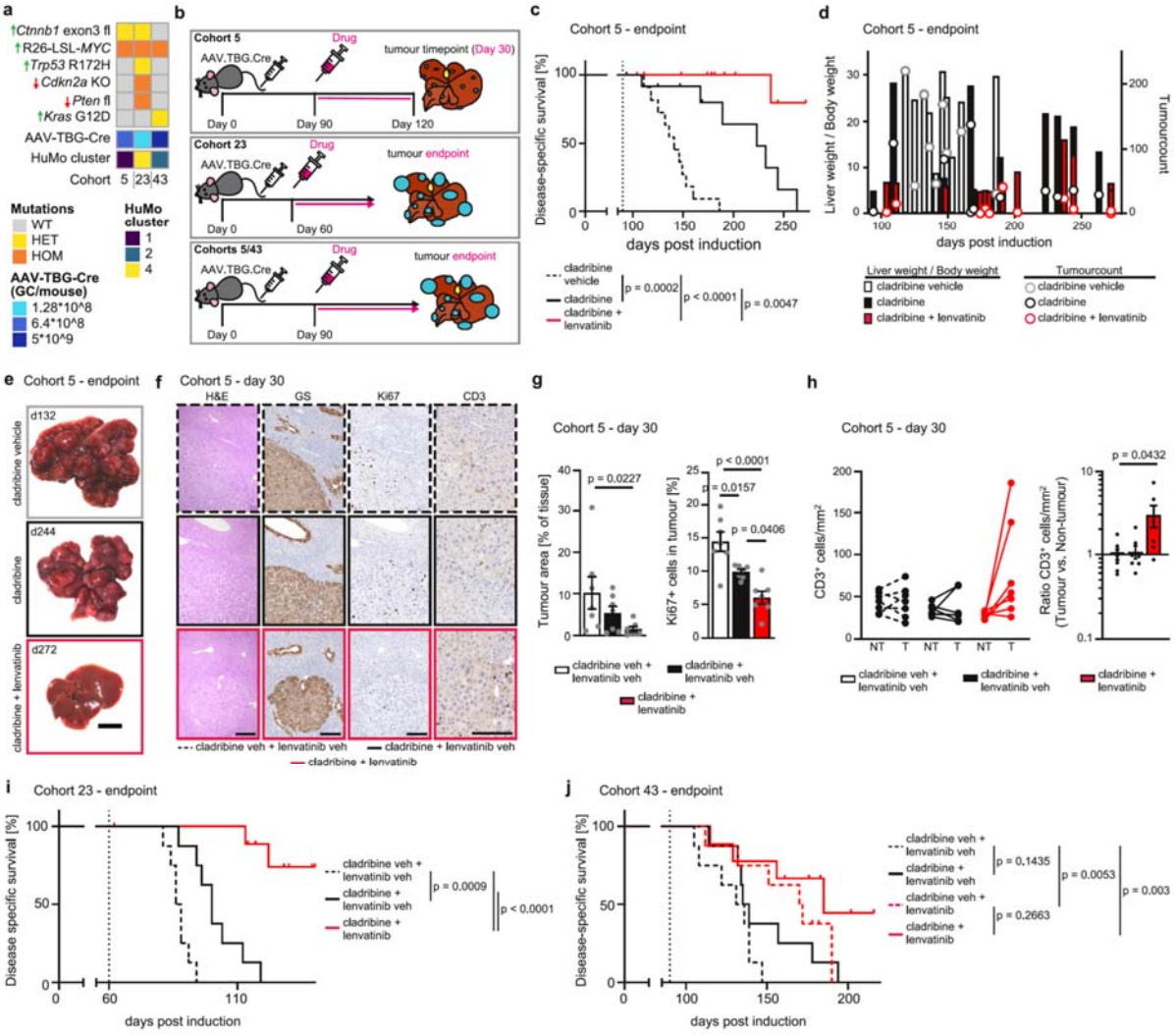

Figure 6: HuMo cluster association is indicative of *in vivo* treatment response to cladribine. (a) Summary of cohorts used in **c-j. (b)** Treatment scheme for **c-j** with drug given from d60 or d90 post induction determined by mean cohort survival. **(c)** Treatment with cladribine alone significantly prolongs disease specific survival in Cohort 5 (BM, male, HuMo 1) mice, and even more when given as combination treatment with lenvatinib. Dotted vertical line indicates treatment start. n = 11 (vehicle), 13 (cladribine, cladribine + lenvatinib). Log rank test. **(d)** Liver weight/ body weight ratio and tumour count over time prove efficacy of cladribine and cladribine + lenvatinib treatment to reduce overall tumour burden. Data shown as bars and symbols for individual mice. n = 10/9 (vehicle), 11/11 (cladribine), 13/12 (cladribine + lenvatinib) for weight ratio/counts. **(e)** Representative images of macroscopic tumour burden of mice treated with vehicle, cladribine, or cladribine + lenvatinib at the indicated days. Scale bar equals 1cm. **(f-h)** Cohort 5 (BM) mice treated with cladribine + lenvatinib have fewer proliferating cells in their tumours and more infiltration of $CD3^+$ T-cells,

but GS expression or general morphology are unaltered when compared at day 30 post treatment start. **(f)** Representative images. Scale bars equal 200µm (H&E, GS, Ki67) or 100µm (CD3). **(g)** Tumour area (based on GS^{+}) and tumour proliferation (assessed by Ki67) are reduced after 30d of cladribine treatment. This is even more pronounced with cladribine + lenvatinib combination treatment. n = 7 (all sample groups). Data shown as mean ± s.e.m. Kruskal-Wallis test with Dunn's correction (Tumour area)/One-way ANOVA with Tukey correction (Ki67). **(h)** Infiltration of $CD3^{+}$ T-cells into the tumour is increased after 30 days of cladribine + lenvatinib treatment. NT = non-tumour tissue and T = tumour tissue are matched. n = 7 (all sample groups). Data shown as mean ± s.e.m. One-way ANOVA with Tukey correction. **(i)** Treatment with cladribine significantly prolongs disease specific survival in Cohort 23 (BM + $Pten^{fl/fl}$ + $Trp53^{R172H/wt}$ + $Cdkn2a^{KO/KO}$, male, HuMo 4) mice, and even more when given as combination treatment with lenvatinib. Dotted vertical line indicates treatment start. n = 9 (cladribine vehicle + lenvatinib vehicle, cladribine + lenvatinib vehicle), 10 (cladribine + lenvatinib). Log rank test. **(j)** Treatment with cladribine does not improve disease specific survival in Cohort 43 ($R26^{LSL\text{-}MYC/LSL\text{-}MYC}$ + $Kras^{G12D/wt}$, male, HuMo 2) mice in contrast to lenvatinib treatment. Combination treatment does not enhance survival beyond lenvatinib monotherapy. Dotted vertical line indicates treatment start. n = 8 (cladribine vehicle + lenvatinib vehicle, cladribine + lenvatinib vehicle, cladribine vehicle + lenvatinib), 9 (cladribine + lenvatinib). Log rank test.

Censored mice in (**c**), (**i**), and (**j**) were sampled for clinically significant weight loss, not clinical tumour endpoint.

Extended Data Figure 1

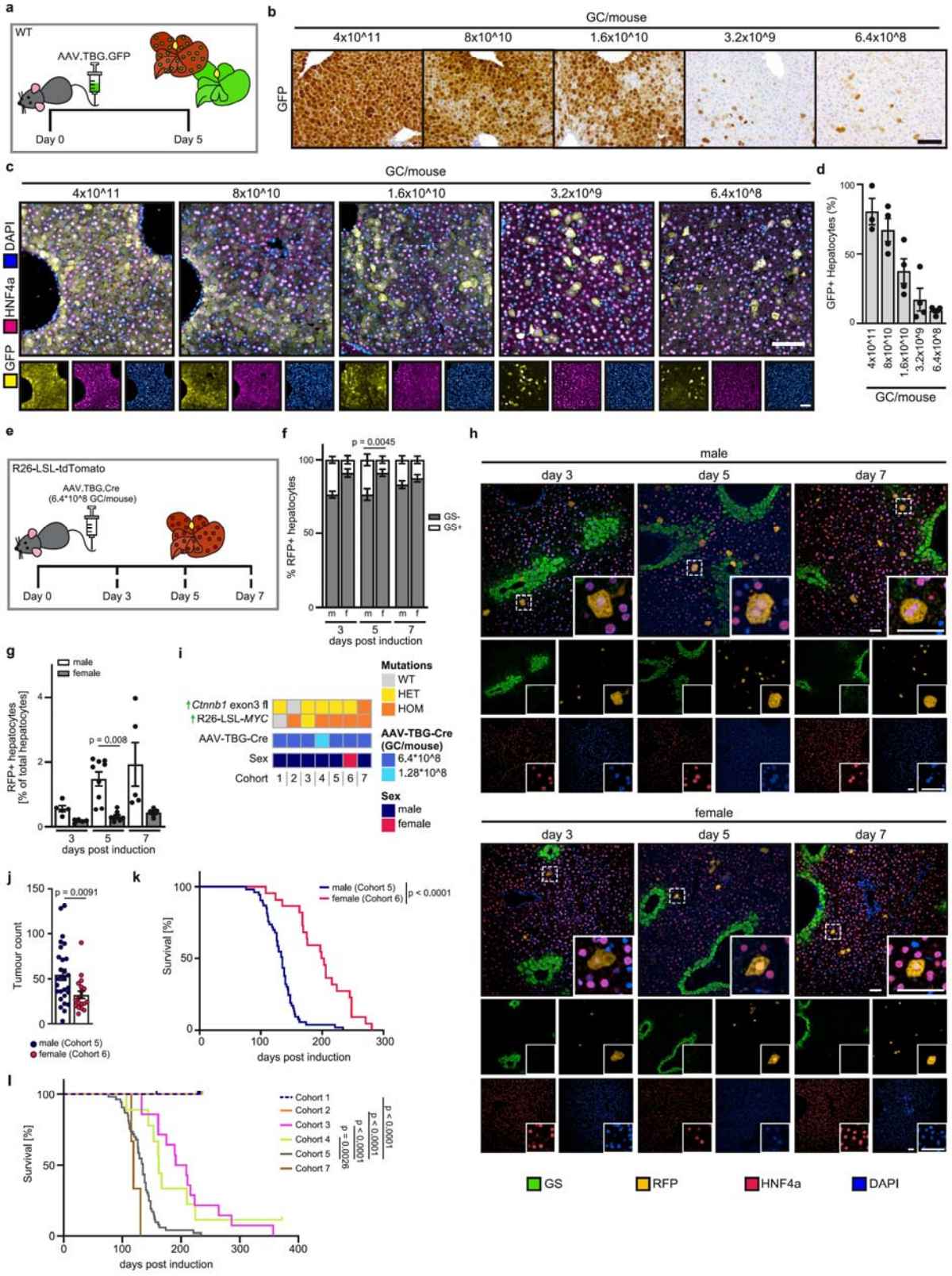

Extended Data Figure 1: Induction of clonal tumour outgrowth of hepatocytes depends on sex and mutational burden. (a) Dose finding for clonal induction using AAV-TBG-GFP. Experimental scheme for **b-d**. **(b)** GFP staining shows a progressive decline in GFP$^+$

hepatocytes with decreasing doses of AAV-TBG-GFP. Scale bar equals 200µm. GC = genomic copies. **(c)** Immunofluorescent staining demonstrates exclusive and dose-dependent targeting of hepatocytes by AAV-TBG-GFP. Individual Channels for GFP (yellow), HNF4a (magenta), DAPI (blue). Scale bar equals 100µm. **(d)** Quantification of c. n = 3-4 mice. Data shown as mean ± s.e.m. **(e)** AAV-TBG-Cre sex-dependent clonal induction variation over time. Experimental scheme for **f-i**. **(f)** Quantification of RFP^+ hepatocytes using the zone 3 marker glutamine synthetase (GS) shows clonal induction within zone 3 and outside zone 3 but no significant zonal expansion over time using a dose of 6.4*10^8 GC/mouse. n = 5 (male d3 + d7, female d3 + d7), 8 (female d5), 9 (male d5). Data shown as mean ± s.e.m. Two-way ANOVA with Tukey correction **(g)** Male mice recombine at a higher rate than female mice after induction with 6.4*10^8 GC/mouse with no additional residual recombination from 5 to 7 days post induction. n = 5 (male d3 + d7, female d3 + d7), 8 (female d5), 9 (male d5). Data shown as mean ± s.e.m. Kruskal-Wallis test with Dunn's correction **(h)** Representative images of Cre-driven recombination rates in males and females on d3, d5, and d7 post induction. Scale Bar equals 50µm. **(i)** Summary of mouse cohorts used in **j-l**. **(j)** A lower induction rate in females leads to a lower tumour burden compared to males with the same mutational background. n = 19 (Cohort 6), 28 (Cohort 5). Data shown as mean ± s.e.m. Unpaired t-test. **(k)** Lower tumour burden due to a lower induction rate causes a prolonged survival in female mice compared to males with the same mutational background. n = 22 (Cohort 6), 53 (Cohort 5). Log rank test. **(l)** Mutational burden and induction dose influence tumour penetrance and survival outcomes. n = 11 (Cohort 1), 8 (Cohort 2), 14 (Cohort 3), 9 (Cohort 4), 53 (Cohort 5 – same data as k), 3 (Cohort 7). Log rank test. All panels: GC = genomic copies.

Please note that individual cohort survival data shown for Cohort 5 and 6 is also shown in Extended Data Fig. 2a to allow direct comparison with data in that figure.

Extended Data Figure 2

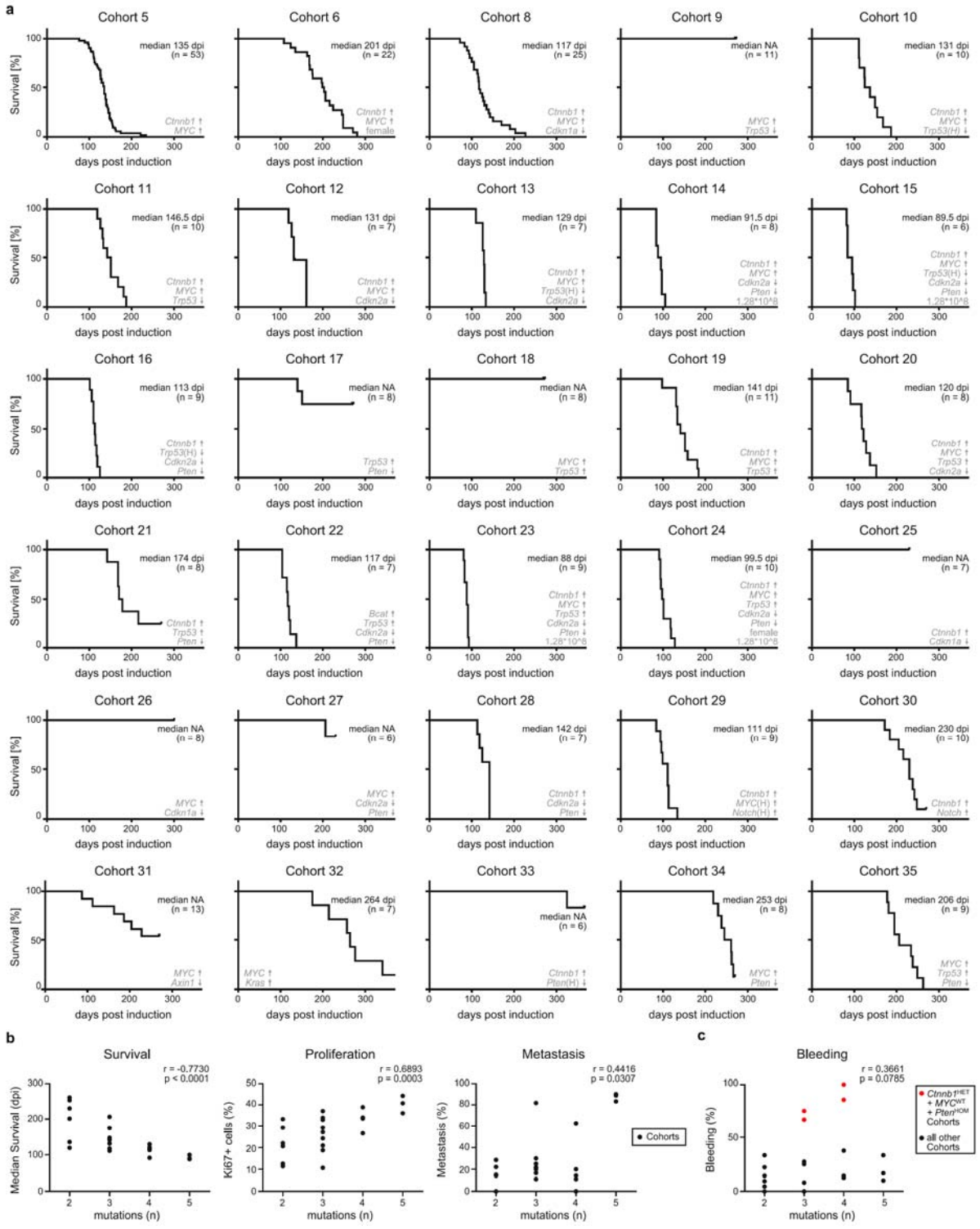

Extended Data Figure 2: Endpoint survival and tumour penetrance varies depending on co-occurrence of mutations. (a) Detailed survival data for summary data shown in **Fig. 1b**. Median survival reported as days post induction (dpi). Number of mice used per cohort as shown in the Figure. All cohorts except Cohort 6 and 24 are male mice. Unless otherwise specified mice were induced with 6.4*10^8 GC/mouse. (H) indicates heterozygosity of an

549 otherwise homozygous allele. **(b)** Correlation analysis of mutational burden and survival,
550 tumour proliferation, and metastasis. n = 7 (2 Mutations), 9 (3 Mutations), 5 (4 Mutations), 3
551 (5 Mutations). Spearman Rank Test. **(c)** Correlation analysis of mutational burden and
552 bleeding. n = 7 (2 Mutations), 9 (3 Mutations), 5 (4 Mutations), 3 (5 Mutations). Spearman
553 Rank Test.
554 Please note that survival data shown for Cohort 5 and 6 are also shown in Extended Data Fig.
555 1l to allow direct comparison with data in that figure.

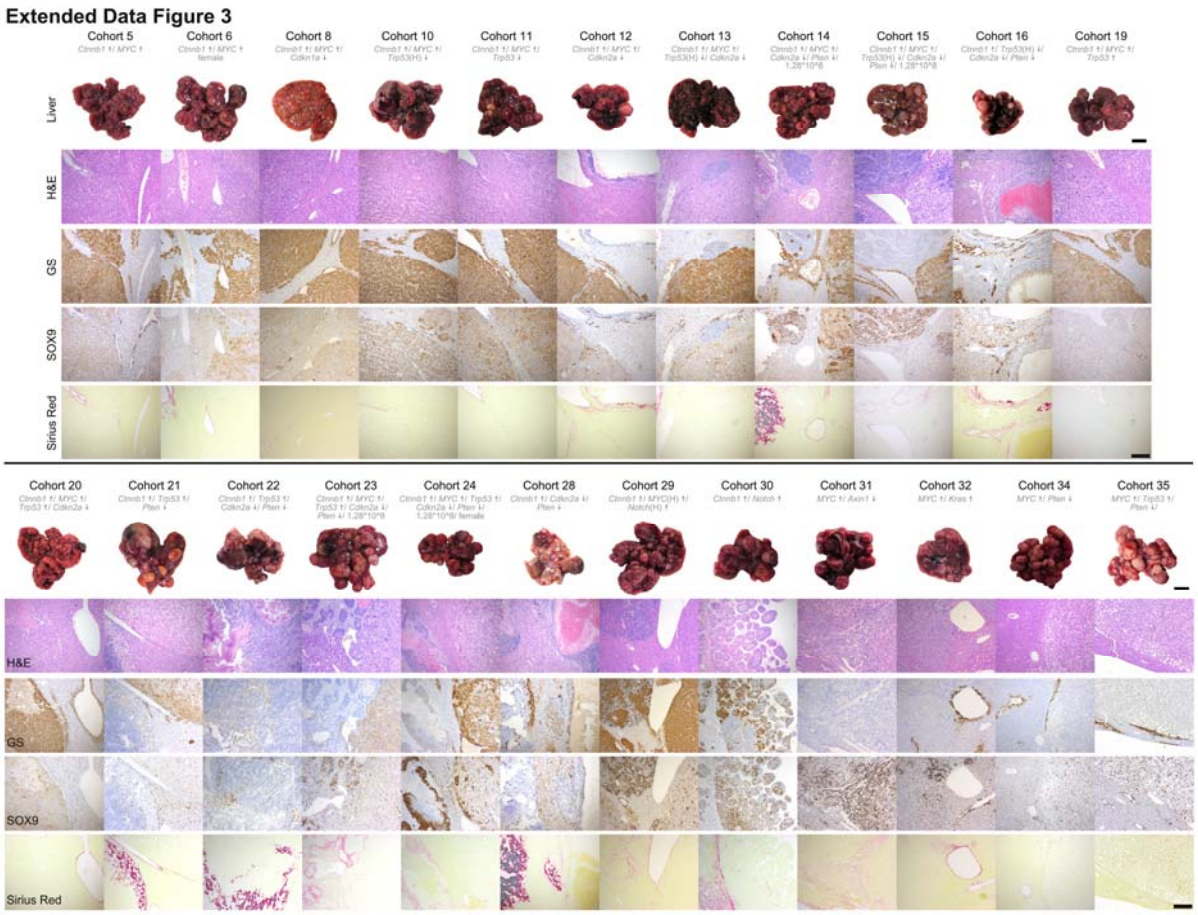

Extended Data Figure 3: Macroscopic and microscopic tumour nodule phenotype reflect the heterogeneity of human HCC. Shown are representative images for each Cohort with staining for general morphology (H&E), glutamine synthetase (GS) for activated beta-catenin signalling, SOX9 as a progenitor marker, and Sirius Red as an indicator for extracellular matrix content in the tumours. All cohorts except Cohort 6 and 24 are male mice. Unless otherwise specified mice were induced with 6.4*10^8 GC/mouse. (H) indicates heterozygosity of an otherwise homozygous allele. Scale bar equals 1cm (macroscopic) or 200µm (microscopic). Macroscopic images and microscopic of H&E and GS for Cohorts 5, 19, 23, 28, 30, and 35 are the same as in Fig. 1c and are shown here to allow direct comparison with data in this figure.

Extended Data Figure 4

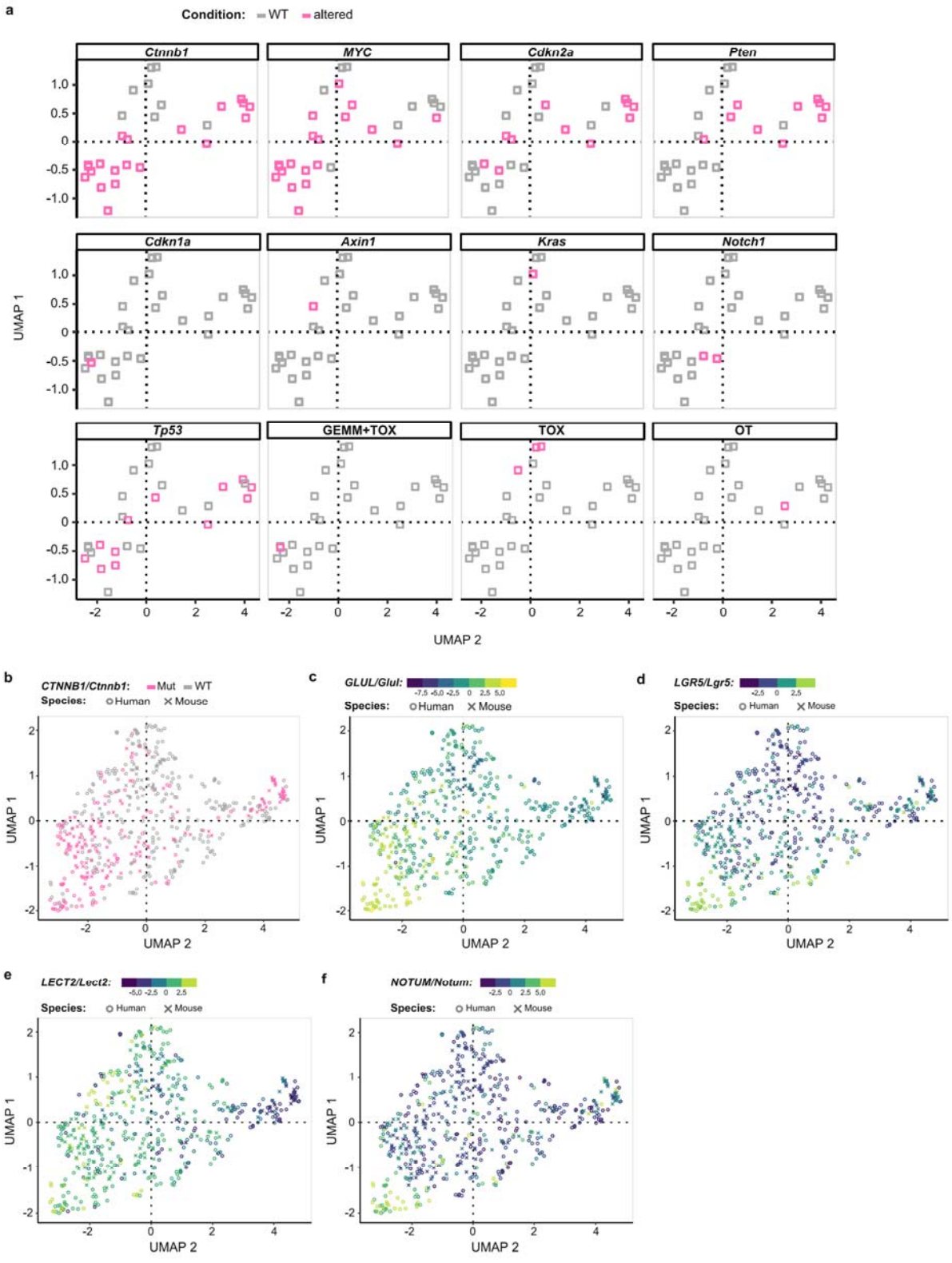

Extended Data Figure 4: Mutational status alone does not explain cluster association. **(a)** UMAPs showing mean distribution of mouse cohorts by specific genetic alterations, carcinogen treatment (TOX), or orthotopic transplant (OT). **(b-f)** Samples with mutated *CTNNB1/Ctnnb1* **(b)** are spread over the whole UMAP spectrum, whereas samples with

expression of beta-catenin pathway downstream targets *GLUL/Glul* **(c)**, *LGR5/Lgr5* **(d)**, *LECT2/Lect2* **(e)**, and *NOTUM/Notum* **(f)** are confined to the lower left quadrant.

Extended Data Figure 5

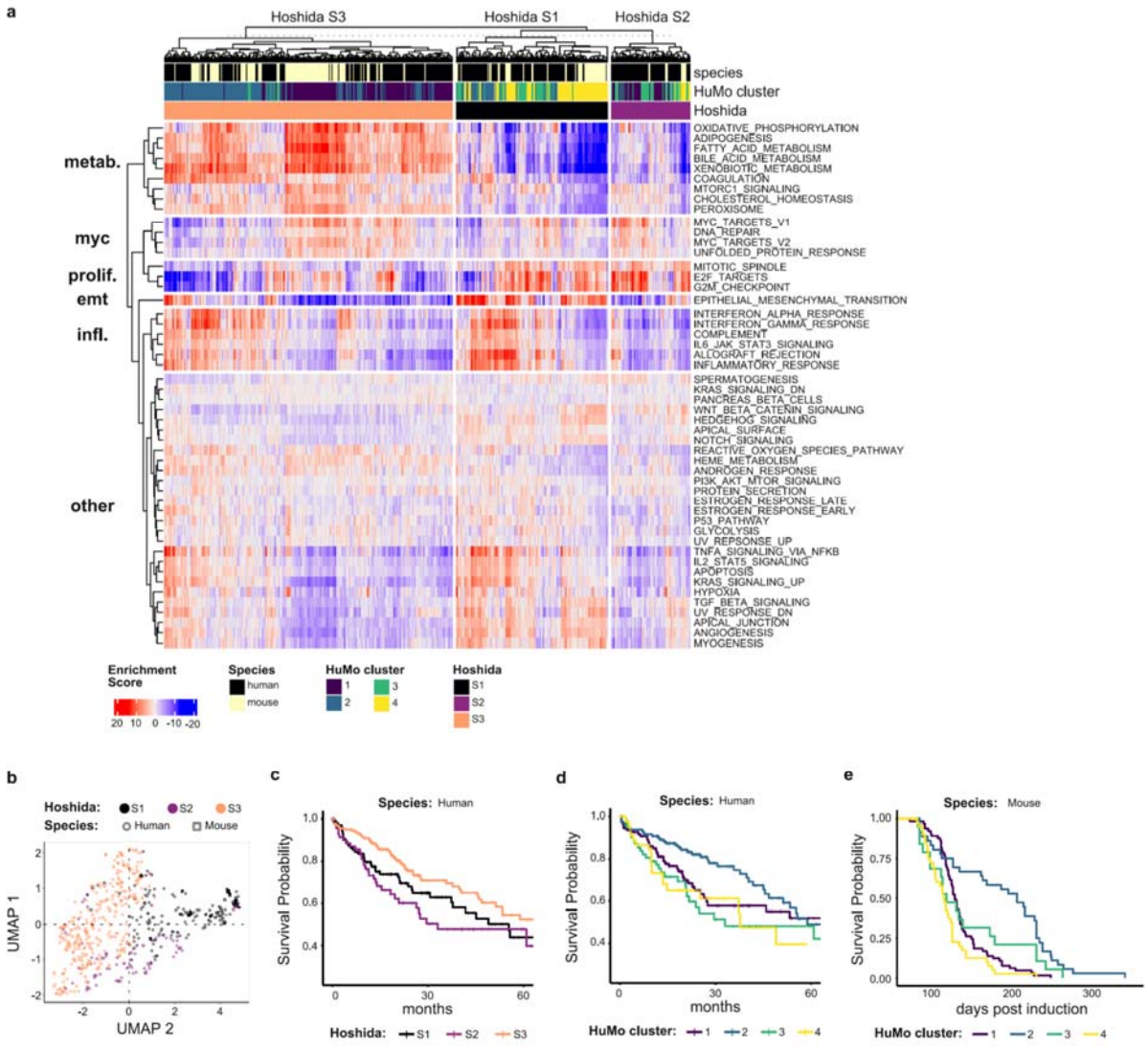

Extended Data Figure 5: Conventional clinically used classifications of human hepatocellular carcinoma fail to cluster TCGA HCC data distinctly. (a) Hallmark pathway-based clustering of the TCGA human hepatocellular carcinoma data set does not reflect previously described and clinically used transcriptional hepatocellular carcinoma subtypes Hoshida S1-S3 **(b)** Distribution of Hoshida S1-S3 subtypes by UMAP **(c)** Survival of TCGA-LIHC cohort by Hoshida subtype. n = 112 (S1), 75 (S2), 185 (S3). **(d)** Survival of TCGA-LIHC cohort by HuMo cluster. n = 119 (HuMo1), 137 (HuMo2), 66 (HuMo3), 50 (HuMo4). **(e)** Survival of all genetically engineered mice based on individual mouse HuMo cluster association. n = 65 (HuMo1), 36 (HuMo2), 19 (HuMo3), 40 (HuMo4).

Extended Data Figure 6

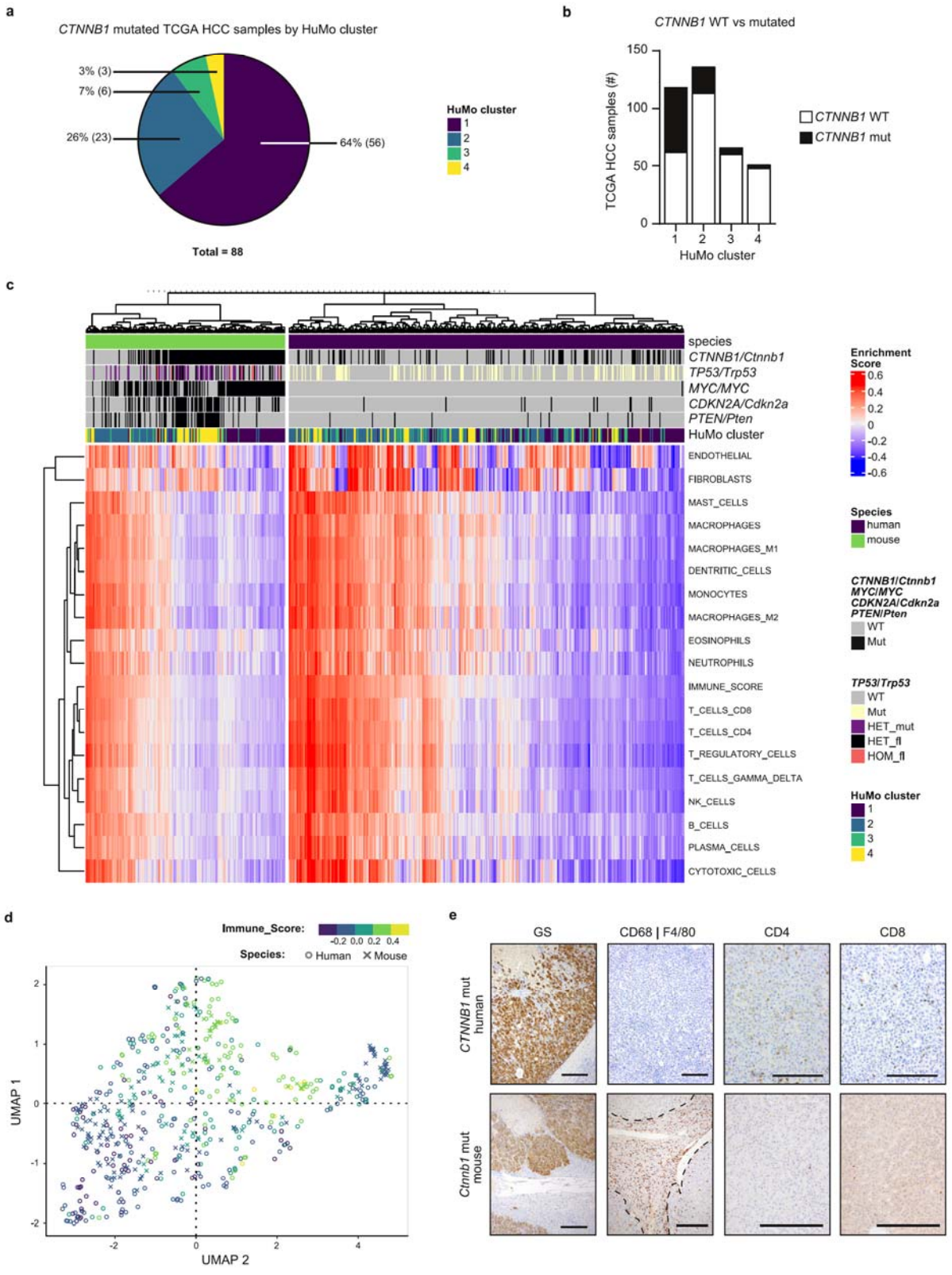

Extended Data Figure 6: Immune-paucity correlates with activation of beta-catenin signalling in HuMo cluster 1. (a) Percentage (total number) of human TCGA HCC samples with mutations in *CTNNB1* associated with each HuMo cluster **(b)** Ratio of wild type and

mutated *CTNNB1* in human TCGA HCC samples within each HuMo cluster **(c)** Detailed immune-pathway analysis shows a clear association of HuMo cluster 1 with immune paucity, whereas HuMo cluster 2 shows the highest association with immune-cell enrichment. **(d)** The immune score is inversely correlated to *GLUL/Glul* expression (**Extended Data Fig. 4b**) and HuMo cluster1 (**Fig, 2b**) as presented by UMAP. **(e)** Both human and mouse samples with activating *CTNNB1/Ctnnb1* mutations show high expression of glutamine synthetase (GS) in the liver tumour tissue as well as very little immune cell infiltration into the tumour of either $CD68^+$|$F4/80^+$ macrophages, or $CD4^+$ or $CD8^+$ T-Cells. Scale bars equal 200µm.

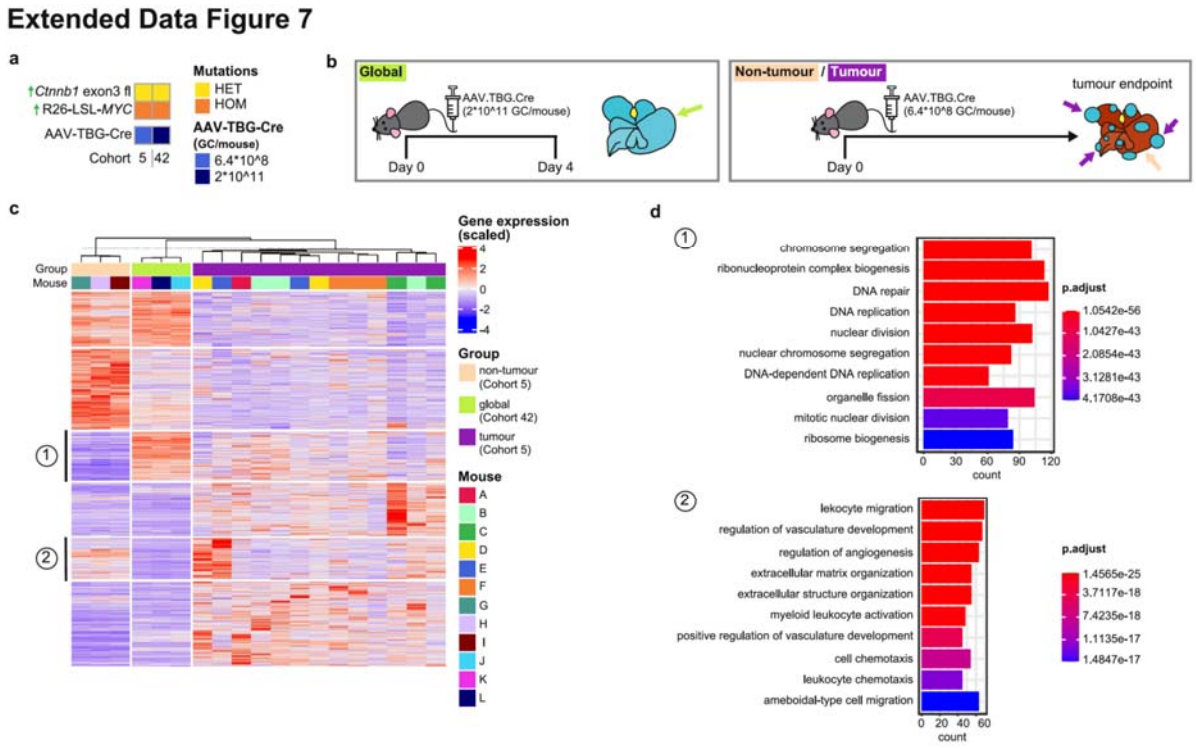

Extended Data Figure 7: Tumours in a mouse model representative of HuMo cluster 1 have mild inter-tumoural and inter-murine heterogeneity but differ greatly from non-tumour tissue or global hepatocytic oncogene induction. (a) Summary of cohorts used in this figure. All mice used in this figure were male. **(b)** Experimental scheme for samples used in **c+d**. **(c)** Heatmap of differentially expressed genes between liver tissue from mice with global hepatocyte induction of altered genes and, non-tumour and tumour, tissue from mice with clonal hepatocyte induction of altered genes. Tumour tissue, despite induction of the same genetic alterations, differs greatly from the global induction group suggesting evolution of induced clones to develop tumours. n = 3 (global and non-tumour), 6 mice with up to 3 tumour samples per mouse (tumour). **(d)** Gene Ontology over-representation analysis shows upregulation of processes associated with oncogenesis in tumour tissue.

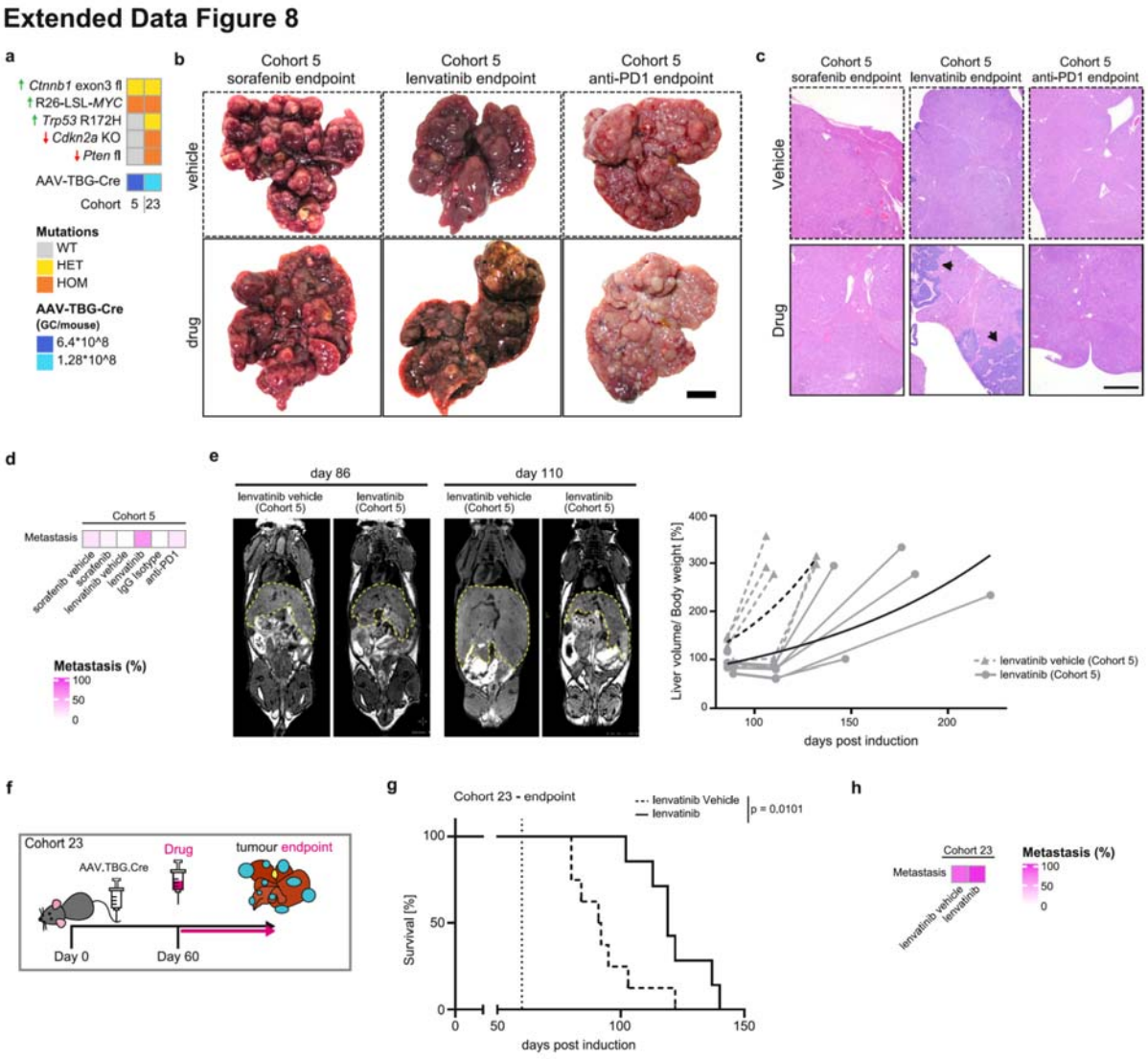

Extended Data Figure 8: Treatment with the tyrosine kinase inhibitor lenvatinib leads to phenotypic changes and increased metastasis. (a) Summary of cohorts used in **b-h**. All mice used in this figure were male. **(b)** Macroscopic liver images of drug and vehicle treated Cohort 5 (BM) mice at endpoint. Scale bar equals 1cm. **(c+d)** Treatment with lenvatinib, but not sorafenib or anti-PD1, results in a more aggressive tumour morphology (indicated by black arrows) and increased number of mice with detectable metastasis at endpoint in Cohort 5 (BM) mice. Scale bar equals 1mm. n = 17 (sorafenib vehicle), 13 (sorafenib), 5 (lenvatinib vehicle + lenvatinib + IgG Isotype), 7 (anti-PD1) **(e)** Non-invasive magnetic resonance imaging of Cohort 5 (BM) mice reveals delayed tumour growth in lenvatinib treated mice with liver volume as a proxy for tumour burden. n = 5 (lenvatinib Vehicle), 6 (lenvatinib). **(f)** Treatment scheme for **g-h** with drug given from d60 post induction to accommodate for faster model progression (**see Extended Data Fig. 2a**). **(g)** Lenvatinib treatment improves endpoint survival in a representative GEMM of HuMo cluster 4 (Cohort 23, BM + *Pten*$^{fl/fl}$ + *Trp53*$^{R172H/wt}$ +

Cdkn2a$^{KO/KO}$). Dotted vertical line indicates treatment start. n = 8 (lenvatinib vehicle), 7 (lenvatinib). Log rank test. **(h)** Cohort 23 (BM + *Pten*$^{fl/fl}$ + *Trp53*$^{R172H/wt}$ + *Cdkn2a*$^{KO/KO}$) mice treated with lenvatinib have increased number of mice with detectable metastasis at endpoint. n = 6 (lenvatinib vehicle), 7 (lenvatinib).

Extended Data Figure 9

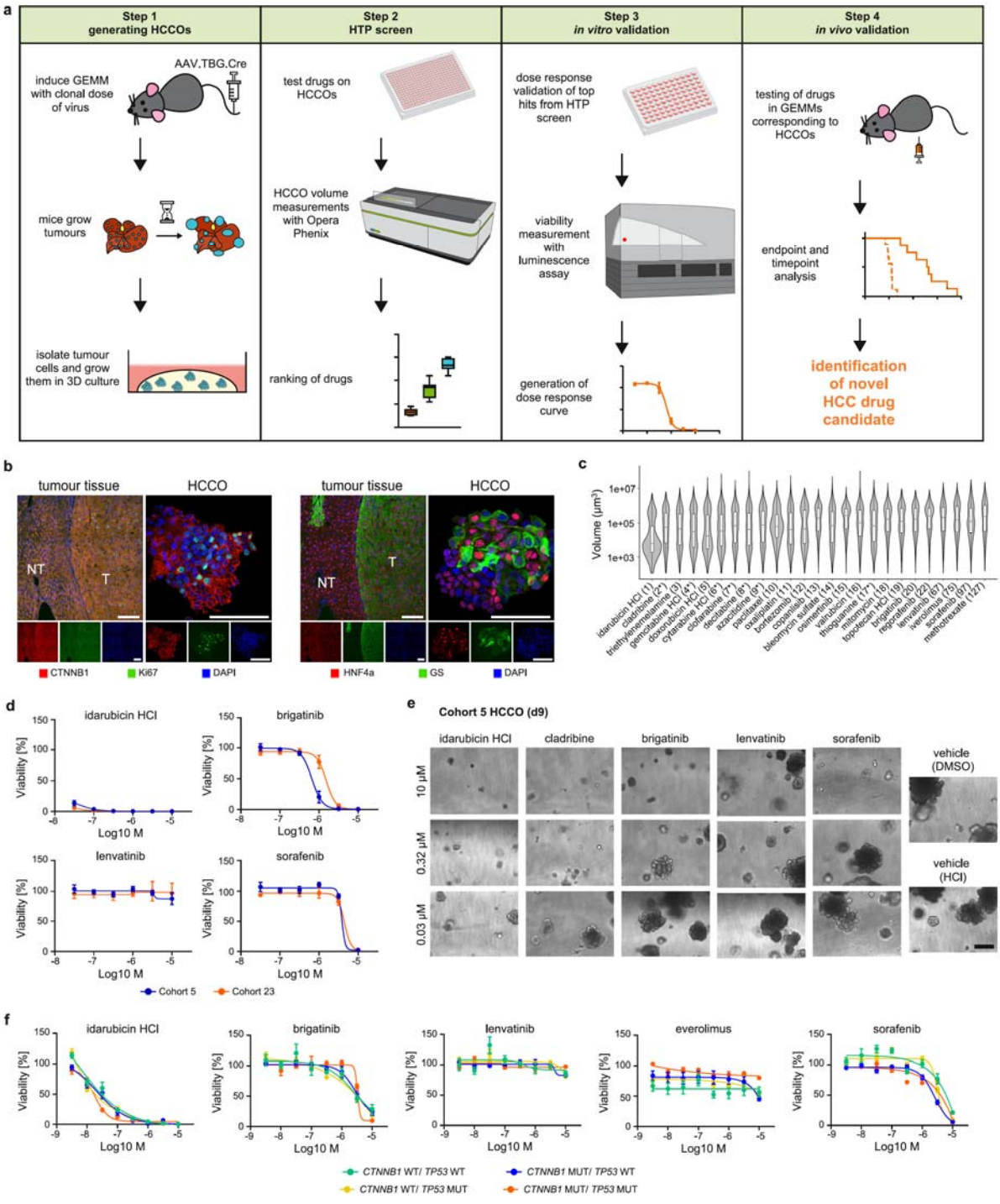

Extended Data Figure 9: A high-throughput tumoroid assay pipeline identifies anti-cancer drugs for repurposing as potential HCC therapy. (a) Schematic of murine HCCO assay pipeline. HTP = high-throughput, GEMM = genetically-engineered mouse model, HCC = hepatocellular carcinoma, HCCOs = HCC organoids. **(b)** HCCOs keep characteristics of primary tumour tissue such as beta-catenin (CTNNB1), glutamine synthetase (GS), proliferation marker Ki67, and differentiation marker HNF4a. Scale bars equal 100µm **(c)**

Volumetric measurements of HCCOs after 9d treatment with indicated drugs. Ranking position in parenthesis. Nucleobase/Nucleoside analogues indicated by asterisks. **(d)** *In vitro* dose-dependency testing of drug efficacy in murine HCCOs validates results from screen. n = 3 (different passages from one HCCO line per named mouse cohort, technical duplicates). Data shown as mean ± s.e.m. **(e)** Representative images of dose-dependent drug effects on murine HCCOs after 9 days of treatment. Scale bar equals 200µm. **(f)** *In vitro* dose-dependency testing of drug efficacy in human HCCOs validates results from screen. n = 3 (different passages from one to ten human HCCO lines per driver combination, see methods for details, technical duplicates). Data shown as mean ± s.e.m.

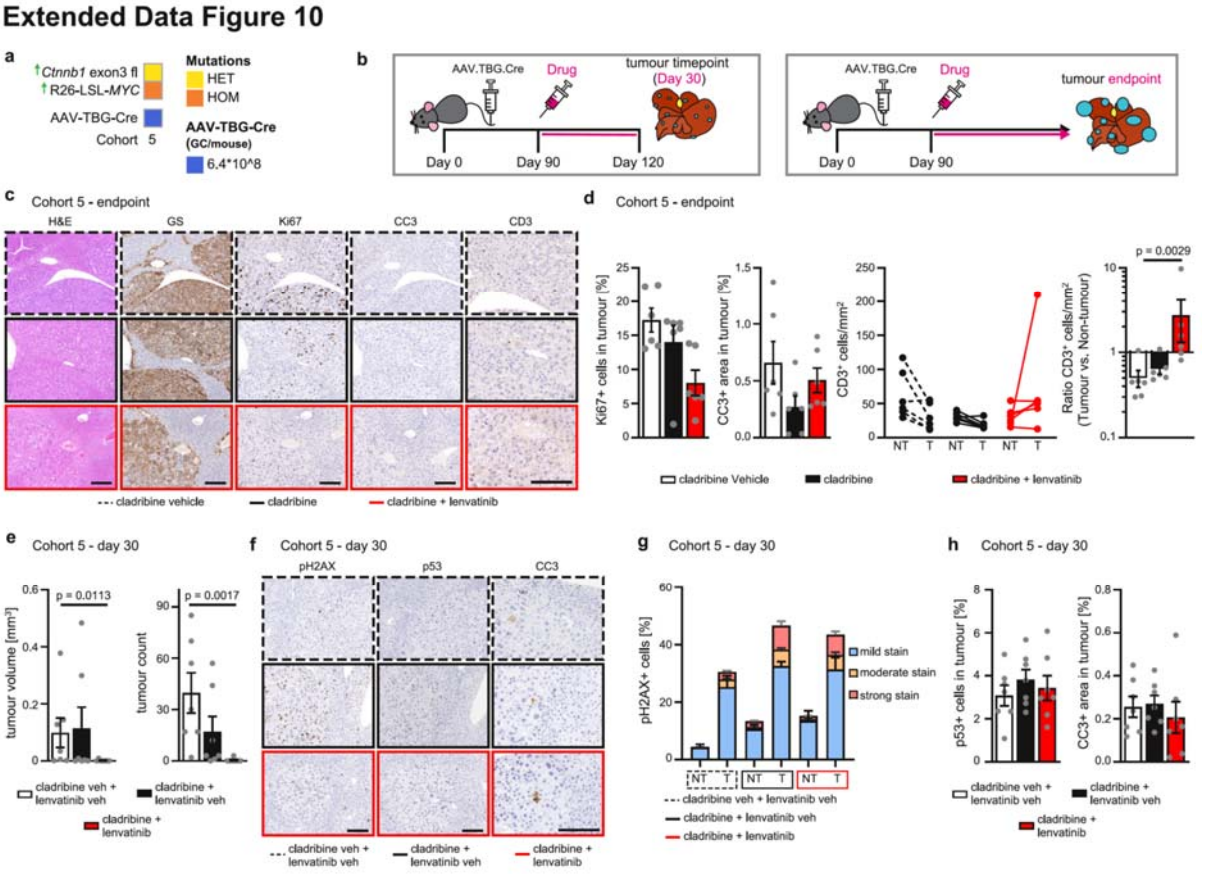

Extended Data Figure 10: Cladribine-induced DNA damage decreases tumour burden by increasing immune cell infiltration and decreasing proliferation but not by upregulating apoptosis. (a+b) Cohort summary and schematic of treatment regimens used in **c-h**. All mice used in this figure were male. **(c+d)** Cohort 5 (BM) mice treated with cladribine + lenvatinib have fewer proliferating cells in their tumours and more infiltration of $CD3^+$ T-cells, but levels of cleaved Caspase 3 (CC3) as well as general morphology are unaltered when compared at endpoint. **(c)** Representative images. Scale bars equal 200µm (H&E, GS, Ki67, CC3) or 100µm (CD3). **(d)** Quantification of Ki67, CC3, and CD3 in matched non-tumour (NT) and tumour (T) tissue. n = 6 (cladribine vehicle, cladribine), 8 (cladribine + lenvatinib, two of the mice did not present with microscopic tumours). Data shown as mean ± s.e.m. Kruskal-Wallis test with Dunn's correction (Ki67, CD3)/One-way ANOVA with Tukey correction (CC3). **(e)** After 30 days on treatment, Cohort 5 (BM) mice on cladribine + lenvatinib combination therapy have smaller and fewer tumours. n = 7 (all sample groups). Data shown as mean ± s.e.m. Kruskal-Wallis test with Dunn's correction. **(f-h)** Cladribine treatment for 30 days, either as monotherapy or combination therapy, induces DNA damage in matched tumour (T) and non-tumour (NT) tissue as determined by phosphorylation of Histone 2AX (pH2AX). This does not result in increased senescence, assessed by p53, or apoptosis, assessed by cleaved caspase 3

(CC3). **(f)** Representative immunohistochemistry images. Scale bars equal 200µm (pH2AX, p53) or 100µm (CC3). **(g)** Quantification of pH2AX in matched non-tumour (NT) and tumour (T) tissue. n = 7 (all sample groups). Data shown as mean + s.e.m. Two-way ANOVA with Tukey correction. **(h)** Quantification of p53 and CC3 tumour tissue. n = 7 (all sample groups). Data shown as mean ± s.e.m. One-way ANOVA with Tukey correction.

Methods

Mice, diets and treatments

All animal experiments were performed in accordance with UK Home Office licences (70/8891, PP0604995, 70/8646, 70/8468, and PP8854860) and in accordance with the UK Animal (Scientific Procedures) Act 1986 and EU direction 2010. They were subject to review by the animal welfare and ethical review board of the University of Glasgow and the University of Newcastle upon Tyne. ARRIVE guidelines were followed for reporting of animal experiments[39]. To minimize pain, suffering, and distress to the animals we used single use needles and non-adverse handling techniques. Mice were housed under controlled conditions (specific pathogen free, 12hr light-dark cycle, 19-22 °C, 45-65% humidity) with access to food and water ad libitum. We added environmental enrichments, in the form of gnawing sticks, plastic tunnels, and nesting material to all cages.

Unless otherwise specified male mice on a mixed background were used. The following transgenic mice strains were used: Gt(ROSA)26Sor$^{tm14(CAG-tdTomato)Hze}$ (R26$^{LSL-Tom}$) [40], Ctnnb1^{tm1Mmt} (*Ctnnb1*^{ex3}) [41], Gt(ROSA)26Sor$^{tm1(MYC)Djmy}$ (R26$^{LSL-MYC}$) [42], Trp53^{tm1Brn} (*Trp53*^{fl}) [43], Trp53^{tm2Tyj} (*Trp53*^{R172H}) [44], Cdkn2a$^{tm1.1Brn}$ (*Cdkn2a*^{KO}) [45], Pten^{tm2Mak} (*Pten*^{fl}) [46], Gt(ROSA)26Sor$^{tm1(Notch1)Dam}$ (R26$^{LSL-NICD}$) [47], Kras^{tm4Tyj} (*Kras*^{G12D}) [48], Cdkn1a^{tm1Led} (*Cdkn1a*^{KO}) [49], Axin1 (*Axin1*^{fl}) [50]. Genotyping was performed by Transnetyx using ear notches taken for identification purposes at weaning (3 weeks of age). Mice were induced between 8 and 12 weeks of age, unless otherwise indicated, with AAV8.TBG.PI.eGFP.WPRE.bGH (AAV8-TBG-GFP) (Addgene, 105535-AAV8), AAV8.TBG.PI.Cre.rBG (AAV8-TBG-Cre) (Addgene, 107787-AAV8) or AAV8.TBG.PI.Null.bGH (AAV8-TBG-Null) (Addgene, 105536-AAV8). Virus was diluted in 100µl PBS to the desired concentration and injected via the tail vein. Unless otherwise specified, mice received a dose of 6.4*10^8 GC/mouse.

For the GEMM+MWD model 6-week old mice were kept on a modified western diet (Envigo -TD.120528) plus sugar water (23.1 g/L fructose and 18.9 g/L glucose) in combination with repeated CCl4 injections (ip, 0.2 µl/g of body weight, Veh: Cornoil) as previously described[51] and were induced with AAV-TBG-Cre at 10 weeks of age.

For the DEN/ALIOS model, C57BL/6 WT mice, were injected with a single dose of DEN (80 mg/kg by i.p. injection) at 14 days of age. Mice were fed ALIOS diet (Envigo, TD.110201) and sugar water (23.1 g/L fructose and 18.9 g/L glucose) from 60 days of age. Mice were harvested at day 284.

For MWD+CCl4 model mice were kept on a modified western diet (Envigo -TD.120528) plus sugar water (23.1 g/L fructose and 18.9 g/L glucose) in combination with repeated CCl4 injections (ip, 0.2 µl/g of body weight, Veh: Cornoil) as previously described[51].

For the streptozotocin (STZ) model, male and female C57BL/6J WT mice were injected with a single dose of STZ (200µg in 0.1M citrate buffer, pH 4.0) subcutaneously at 2 days of age. Mice were fed high-fat diet (TestDiet 58R3, cat.no. 1810835) from 30 days of age. All STZ–HFD-treated liver showed pale yellow colour at 6 week, mild swelling at 8 week, granular surface at 12 week and tumour protrusion at 20 weeks of age[52] . Mice were harvested between 17 and 35 weeks of age.

For the orthotopic model, Hep-53.4 cells (female C57BL/6J hepatoma cell line) were injected intrahepatic into the left lobe of male C57BL/6J mice. The procedure was performed under isoflurane general anaesthesia. Analgesia were given to the mice for pain management. Mice were harvested at 28 days post implantation or left to reach an approved humane endpoint.

For therapeutic intervention drugs were given at 60 days or 90 days post induction as indicated in the figures. The following drugs were used: Sorafenib (LC Laboratories S8502, daily, OG, 45mg/kg, Veh: 50%Chremophor/50% EtOH - then before dosing 3 part H_2O added), Lenvatinib (SelleckChem S1164 [endpoint studies] or Eisai [monotherapy timepoint studies], daily, OG, 10mg/kg, Veh: 3mM HCl), anti-PD1 (Biolegend RMP1-14; 2x week, IP, 200 µg, Veh: PBS; Ctrl: IgG, Biolegend RTK2758), Cladribine (SelleckChem S1199, daily, IP, 20mg/kg, Veh: PBS). To help with drug-induced weight loss, mice on Cladribine treatment received irradiated peanuts and sunflower seeds as diet supplements. If mice reached 83% of weight at treatment start cladribine treatment was withheld until they gained weight to at least 90% of weight at treatment start. Mice who dropped below 80% of weight at treatment start were sampled according to license limitations. Confounding factors (e.g. litter mates, induction date) were taken into consideration when allocating mice into groups but mice were not randomised using a specific method. Mice who presented with a visible tumour before treatment start were excluded from the experiments as per *a priori* established criteria. Animal technicians dosing the mice were blinded to the genotype of the mice.

The number of biological replicates ≥ 3 mice per cohort for all experiments. See Figure legends and Extended Data Table 1 for details.

Animal tissue harvesting

GEMMs were sampled at specific time points or at endpoint. Endpoint was defined as having reached a liver weight/ body weight ratio of >20% or having adverse side effects from the

tumour, such as tumour haemorrhaging. Mice who died of tumour haemorrhaging were included in survival analysis but not in any downstream analysis. Tumours were measured macroscopically using digital callipers and visible tumours were counted. Images of whole livers were taken with a Canon PowerShot G9X camera with a ruler present in each picture. Tissue was either sampled in neutral buffered saline containing 10% formaldehyde or snap frozen on dry ice.

Histology and immunohistochemistry

Liver, tumour, and lung-tissues were fixed using neutral buffered saline containing 10% formaldehyde, dehydrated and embedded in paraffin, and cut into 4 μm-thick sections. Sections were dewaxed and stained with haematoxylin-eosin or Sirius Red using standard protocols. Additional sections were stained immunohistochemically using the primary antibodies detailed in **Extended Data Table 3**. Primary antibodies were detected by HRP-labelled secondary antibodies and subsequently stained using a peroxidase DAB kit (Vector Laboratories, SK-4100) with haematoxylin as a counterstain (IHC) or by fluorescent-labelled secondary antibodies (Invitrogen) with DAPI used as counterstain (SouthernBiotech, 0100-20) (IF).

Microscopy and quantitative analysis of immunohistochemistry

Images were obtained on a Zeiss Axiovert 200 microscope using a Zeiss Axiocam MRc camera. For image analysis, stained slides were scanned using a Leica Aperio AT2 slide scanner (Leica Microsystems, UK) at 20x magnification. Quantification of blinded, stained sections (GS, Ki67, CC3, CD3, yH2AX, p53) was performed using the HALO image analysis software (V3.1.1076.363, Indica Labs).

Lungs were microscopically analysed for the presence of extrahepatic HCC spread by examining H&E and GS sections. Metastasis was scored binary as detected or not-detected but was not analysed in respect to individual metastasis burden per mouse.

Images for tissue comparison to HCCOs were taken on a Zeiss 710 confocal microscope.

Tumour scoring

H&E-stained sections and tumours were additionally assessed by a consultant liver histopathologist and UK liver pathology External Quality Assessment scheme member (T.J.K.) working in the national liver transplant centre. All assessment was undertaken blind to all other data, including genotype and sampling times. An initial screen of the first available 135 cases

was made to identify prominent histological features in lesional and non-lesional liver that could be semi-quantitatively assessed.

Accepting the inherent limitations of semi-quantitative subjective histological assessment but using a single observer to remove inter-observer considerations, semi-quantitative/ordinal scoring systems were created for lesional and non-lesional features. Slides containing transections of whole lobes from each animal were assessed as a whole, giving an overall score or impression rather than scoring on an individual-lesion basis.

Non-lesional liver was scored for steatosis (none, focal, abundant) and lobular inflammation (none, focal, abundant). A minority of slides included insufficient non-lesional liver for assessment.

For lesional assessment, the presence of glandular tumour i.e. meriting designation as adenocarcinoma (none, focal, extensive) and undifferentiated carcinoma (none, focal, abundant, exclusive) were assessed first. All hepatocellular neoplastic lesions had the morphological and cytological appearances of malignancy i.e. hepatocellular carcinoma. In all cases where there was hepatocellular carcinoma the following features were assessed using the categories in parentheses: lesional pattern (any from nested, trabecular, solid), lesional steatosis (none, focal, abundant), lesional cell ballooning (none, focal, abundant), intra-lesional inflammation (none, focal, abundant), lesional necrosis (none, focal, confluent, extensive), lesional cell apoptosis (none, focal, many), intra-lesional peliosis (none, focal, abundant), lesional nuclear grade (low – minimal/low pleomorphism, high – highly pleomorphic).

Quantitative analysis of fluorescent immunohistochemistry

Fluorescent tiled images were generated on an Opera Phenix High-Content Screening System (Perkin Elmer) at 20x magnification. Fluorescence was detected using the same settings throughout. Consecutive, non-overlapping fields were analysed blindly using Columbus Image analysis software (2.8.0.138890, Perkin Elmer). Positivity gating thresholds were defined using negative controls. For representative images, processing adjustments were performed equally.

Whole tumour RNA-Sequencing

Whole tumour and healthy tissue was snap frozen and stored at -80C. To cover the breadth of our models, for each cohort tissue from the shortest and longest surviving mouse as well as tissue from mice with survival closest to median cohort survival was chosen. Tissue was homogenized using the Precellys Evolution homogenizer and bulk RNA was isolated using a Trizol (Invitrogen) extraction protocol according to the manufacturer's instructions. RNA

quality and quantity was analysed on a Nanodrop 2000 (Thermo Fisher Scientific) and an Agilent 2200 TapeStation (D1000 screentape). Only samples with a RIN value >7 were used for library preparation. Libraries were prepared using a Lexogen QuantSeq FWD Kit (Disease positioning) or the Illumina TruSeq stranded mRNA Kit (Tumour heterogeneity). Library quality and quantity were assessed using 2200 TapeStation (Agilent) and Qubit (ThermoFisher Scientific). The libraries for the disease positioning were sequenced by Novogene Europe. The libraries for the tumour heterogeneity were run on an Illumina NextSeq 500 using the High Output 75 cycles kit (2x36cycle paired end reads).

Mapping of RNASeq expression data

Quality checks and trimming on the raw RNASeq data files were done using FastQC version 0.11.9 (https://www.bioinformatics.babraham.ac.uk/projects/fastqc/), FastP version 0.20.1 [53], MultiQC version 1.9 [54], and FastQ Screen version 0.14.0 [55]. RNA-Seq paired-end reads were mapped to the GRCm39.103 version of the Mus musculus genome and annotation[56] using STAR version 2.7.8a [57]. Expression levels were determined by FeatureCounts from the Subread package version 2.0.1 [58].

Computational disease positioning based on human TCGA data

TCGA data were downloaded using GenomicDataCommons R package (version 1.12.0, https://bioconductor.org/packages/GenomicDataCommons)[59]. TCGA "HTSeq – counts" and corresponding clinical annotations. TCGA mutational data were downloaded using maftools (version 2.4.2)[60]. Both human and mouse RNASeq counts were normalised using VST from DESeq2 package[61] and then centred within a sample. Genes were reduced to those with direct one-to-one gene mapping between human and mouse genomes established by Ensembl, as retrieved from biomaRt package[62,63]. Singular-value decomposition (SVD) of the human data was performed followed by matrix factorisation of both the human and mouse data into a 100-rank human space. UMAP of the combined dataset was executed using R package uwot (version 0.1.11, https://CRAN.R-project.org/package=uwot). An adjacency matrix was constructed from a nearest neighbours search (RANN package version 2.6.1, https://CRAN.R-project.org/package=RANN) of the human & mouse SVD objects for clustering analysis. R package igraph[64] was used to construct a graph object and community structure was determined using Louvain clustering.

ssGSEA analysis was performed using R package corto[65] with the Hallmark gene-set[66,67] downloaded using msigdbr (version 7.4.1. https://CRAN.R-project.org/package=msigdbr).

Hoshida[21] (also downloaded utilising msigdbr), subclass classification was determined by the highest enriched subclass. Tumour immune cell estimation performed using ConsensusTME[68].

Visualisation of data by a combination of ComplexHeatmap[69], ggplot2[70], cowplot (version 1.1.1. https://CRAN.R-project.org/package=cowplot), and viridis[71] packages.

Human H&E stained tissue sections were obtained from the TCGA collection (https://portal.gdc.cancer.gov/)

Differential expression analysis for inter-tumoural heterogeneity

Genes were restricted to those with significance in all comparisons (with significance defined as adjusted p-values <0.05 and log2FC >1). Data were scaled and visualised using ComplexHeatmap[69] package. Gene Ontology over-representation analysis was performed using the clusterProfiler[72] package.

Human sample ethical approval

The use of consenting patients' tissues surplus to diagnostic requirements for research purposes was approved by the Newcastle and North Tyneside Regional ethics committee, the Newcastle Academic Health Partners Bioresource (NAHPB) and the Newcastle upon Tyne NHS Foundation Trust Research and Development (R&D) department, in accordance with Health Research Authority guidelines. (References 10/H0906/41; NAHPB Project 48; REC 12/NE/0395; R&D 6579; Human Tissue Act license 12534).

Magnetic resonance imaging (MRI)

MRI scans were performed on liver tumour bearing mice using a nanoScan® imaging system (Mediso Medical Imaging Systems, Hungary). Mice were anaesthetised and maintained under inhaled isoflurane anaesthesia (induction 4-5% v/v; maintenance 1.5-2.0% v/v) in 95% oxygen during the entire imaging procedure. Whole body T1-weighted Gradient Echo (GRE) 3D Coronal/Sagittal MRI Sequences [Echo time (TE) 3.8msec, Repetition time (TR) 20msec, Flip Angle 30 degrees, and slice thickness 0.50mm] were used to obtain MRI images. For quantification of scans, volume-of-interests (VOIs) were manually drawn around the liver region on MRI scans by visual inspection using VivoQuant software (version 4.0, InviCRO LLC, MA). For each scan, separate VOIs were prepared to adjust for the position and angle of each mouse on the MRI scanner and their tumour size.

Murine HCCO culture, drug screening, and imaging

HCCOs were extracted and cultured as previously described[26,73], with the exception that HCCOs from mice with activated beta-catenin signalling were cultured in the absence of Wnt and Rspo-1. All murine HCCO cultures were regularly tested for mycoplasma.

For the high-throughput screen Cohort 5 (BM) HCCOs were dissociated with TrypLE and plated at a density of 1×10^3 cells in 10 µL BME in pre-warmed 384-well plates (Greiner BioOne, 781091) five days before adding the drugs. On day 0, a panel of 147 FDA-approved oncology drugs (AOD IX- acquired June 2019, https://dtp.cancer.gov/organization/dscb/obtaining/available_plates.htm) was added at a final concentration of 10µM. Staurosporin was used as an internal positive control, DMSO and untreated cells were used as an internal negative control. Medium was changed on day 4 and the compounds were freshly added. Incucyte NucLight Rapid Red (Sartorius, #4717) was added on day 6 and cells were imaged using the Opera Phenix High-Content Screening System (Perkin Elmer) on day 9. Volumes were determined using Icy BioImage software (https://icy.bioimageanalysis.org)[74]. The experiment was performed twice (using different passages from one HCCO line) in technical quadruplicates.

For the drug dose response curves screen HCCOs (1 line per cohort) were dissociated with TrypLE and plated at a density of 1×10^3 cells in 10 µL Matrigel (Corning, #356231) in pre-warmed 96-well plates (Greiner BioOne, 655098). The treatment schedule was the same as for the HTP screen, except the medium was changed and fresh drugs added on day 3 and 7. Drugs and concentrations are shown in the figures. Drugs were purchased from Selleckchem, dissolved in DMSO to 10 mM, aliquoted and stored at -20°C. Cell viability was measured on day 9 using CellTitre-Glo 3D reagent (Promega, G9682) according to the manufacturer's instructions. Luminescence was measured on a Spark Microplate Reader (Tecan). Results were normalized to vehicle. Curve fitting and IC50 calculation was performed using a nonlinear regression equation. All experiments were performed in duplicate and at least three times using different passages from one HCCO line per Cohort.

Images of HCCOs were taken on an Olympus CKX41 with a Qimaging Retiga Exi Fast 1394 camera.

For IF HCCOs were washed with ice-cold PBS, fixed with 4%PFA and permeabilised with 0.2% Triton X-100. Antibodies are listed in Extended Data Table 3. Images were taken with a Zeiss 710 confocal microscope.

Human HCCO culture and drug screening

Human HCCOs were derived from liver cancer needle-biopsies or liver resections as described before[27]. The following human HCCO lines were used: D386-O and D953-O (CTNNB1 WT, TP53 WT); C948-O, C949-O and D455-O (CTNNB1 MUT, TP53 WT); C655-O, C798-O, C975-O, D045-O, D046-O, D324-O, D803-O, D804-O, D876-O and R035-O (CTNNB1 WT, TP53 MUT); D359-O (CTNNB1 MUT, TP53 MUT).

For expansion, the human HCCOs were seeded into reduced growth factor BME2 (R&D Systems, 3533-005-02), and cultured in expansion medium (EM): advanced DMEM/F-12 (Gibco, Cat. No. 12634010) supplemented with 1x B-27 (Gibco, Cat. No. 17504001), 1x N-2 (Gibco, Cat. No. 17502001), 10 mM Nicotinamide (Sigma, Cat. No. N0636), 1.25 mM N-Acetyl-L-cysteine (Sigma, Cat. No. A9165), 10 nM [Leu15]-Gastrin (Sigma, Cat. No. G9145), 10 µM Forskolin (Tocris, Cat. No. 1099), 5 µM A83-01 (Tocris, Cat. No. 2939), 50 ng/ml EGF (Peprotech, Cat. No. AF-100-15), 100 ng/ml FGF10 (Peprotech, Cat. No. 100-26), 25 ng/ml HGF (Peprotech, Cat. No. 100-39), 10% RSpo1-conditioned medium (v/v, homemade). HCCOs were passaged after dissociation with 0,25% Trypsin-EDTA (Gibco). All human HCCOs were regularly tested for Mycoplasma contamination with the MycoAlert™ Mycoplasma detection kit (Lonza, Cat. No. LT07-118).

Drugs were purchased from ApexBio and Selleckchem, dissolved in DMSO to 10 mM, aliquoted and stored at -20°C. For the screening, human HCCOs were dissociated with 0.25% Trypsin-EDTA (Gibco) to single cells and 1×10^3 cells per well were plated in a 384-well plate (Greiner BioOne, 781986) on a layer of BME2 (R&D Systems, 3533-005-02) previously diluted with EM (50:50 v/v). Cells were cultured for 3 days without treatment to allow for organoid formation. At day 3, an 8-point half-log dilution series of each compound (ranging from 10 µM to 0,00316 µM) was added using a Tecan D300e. Cell viability was measured after 5 days of treatment using CellTiter-Glo 3D reagent (Promega, G9682). Luminescence was measured on a Synergy H1 Multi-Mode Reader (BioTek Instruments). Results were normalized to vehicle (DMSO). The maximal DMSO concentration was 0.2%. Curve fitting was performed using Prism (GraphPad) software and the nonlinear regression equation. Results are shown as mean ± s.e.m.

Quantification and statistical analysis

Statistical analyses were performed using GraphPad Prism software (v9 GraphPad Software, La Jolla, CA, USA) and R (version 4.0.2 and higher) with statistical tests as indicated in the

Figure legends. Data were tested for normal distribution. All performed t-tests were two-tailed. P-values are included in figures.

Figures were assembled using Scribus v1.4.8 (https://www.scribus.net/). Images were processed using Gimp v2.10.14 (https://www.gimp.org/).

HCCO availability

Tumour derived murine HCCOs (available from all GEMMs) will be shared upon reasonable request.

Data availability

All data will be deposited with accession codes, unique identifiers or web links for publicly available datasets provided before publication.

Code availability

Scripts used for disease positioning is available at https://github.com/Beatson-CompBio (full project link will be made available before publication)

References

1. Sung, H. *et al.* Global Cancer Statistics 2020: GLOBOCAN Estimates of Incidence and Mortality Worldwide for 36 Cancers in 185 Countries. *CA. Cancer J. Clin.* **71**, 209–249 (2021).
2. Llovet, J. M. *et al.* Hepatocellular carcinoma. *Nat. Rev. Dis. Primer* **7**, 6 (2021).
3. Brunner, S. F. *et al.* Somatic mutations and clonal dynamics in healthy and cirrhotic human liver. *Nature* **574**, 538–542 (2019).
4. Ally, A. *et al.* Comprehensive and Integrative Genomic Characterization of Hepatocellular Carcinoma. *Cell* **169**, 1327-1341.e23 (2017).
5. Harding, J. J. *et al.* Prospective Genotyping of Hepatocellular Carcinoma: Clinical Implications of Next-Generation Sequencing for Matching Patients to Targeted and Immune Therapies. *Clin. Cancer Res.* **25**, 2116–2126 (2019).
6. Pfister, D. *et al.* NASH limits anti-tumour surveillance in immunotherapy-treated HCC. *Nature* **592**, 450–456 (2021).
7. Bresnahan, E., Ramadori, P., Heikenwalder, M., Zender, L. & Lujambio, A. Novel patient-derived preclinical models of liver cancer. *J. Hepatol.* **72**, 239–249 (2020).

8. Llovet, J. M. *et al.* Sorafenib in Advanced Hepatocellular Carcinoma. *N. Engl. J. Med.* **359**, 378–390 (2008).
9. Kudo, M. *et al.* Lenvatinib versus sorafenib in first-line treatment of patients with unresectable hepatocellular carcinoma: a randomised phase 3 non-inferiority trial. *The Lancet* **391**, 1163–1173 (2018).
10. Finn, R. S. *et al.* Atezolizumab plus Bevacizumab in Unresectable Hepatocellular Carcinoma. *N. Engl. J. Med.* **382**, 1894–1905 (2020).
11. Dow, M. *et al.* Integrative genomic analysis of mouse and human hepatocellular carcinoma. *Proc. Natl. Acad. Sci.* **115**, E9879–E9888 (2018).
12. Molina-Sánchez, P. *et al.* Cooperation Between Distinct Cancer Driver Genes Underlies Intertumor Heterogeneity in Hepatocellular Carcinoma. *Gastroenterology* **159**, 2203-2220.e14 (2020).
13. Guo, L. *et al.* Single-Cell DNA Sequencing Reveals Punctuated and Gradual Clonal Evolution in Hepatocellular Carcinoma. *Gastroenterology* **162**, 238–252 (2022).
14. Paris, J. & Henderson, N. C. Liver zonation, revisited. *Hepatology* hep.32408 (2022) doi:10.1002/hep.32408.
15. Wu, W. *et al.* Pattern of distant extrahepatic metastases in primary liver cancer: a SEER based study. *J. Cancer* **8**, 2312–2318 (2017).
16. Galle, P. R. *et al.* EASL Clinical Practice Guidelines: Management of hepatocellular carcinoma. *J. Hepatol.* **69**, 182–236 (2018).
17. McInnes, L., Healy, J. & Melville, J. UMAP: Uniform Manifold Approximation and Projection for Dimension Reduction. (2018) doi:10.48550/ARXIV.1802.03426.
18. Donehower, L. A. *et al.* Integrated Analysis of TP53 Gene and Pathway Alterations in The Cancer Genome Atlas. *Cell Rep.* **28**, 1370-1384.e5 (2019).
19. Müller, M., Bird, T. G. & Nault, J.-C. The landscape of gene mutations in cirrhosis and hepatocellular carcinoma. *J. Hepatol.* **72**, 990–1002 (2020).
20. Blondel, V. D., Guillaume, J.-L., Lambiotte, R. & Lefebvre, E. Fast unfolding of communities in large networks. *J. Stat. Mech. Theory Exp.* **2008**, P10008 (2008).
21. Hoshida, Y. *et al.* Integrative Transcriptome Analysis Reveals Common Molecular Subclasses of Human Hepatocellular Carcinoma. *Cancer Res.* **69**, 7385–7392 (2009).
22. Sia, D. *et al.* Identification of an Immune-specific Class of Hepatocellular Carcinoma, Based on Molecular Features. *Gastroenterology* **153**, 812–826 (2017).

998 23. Montironi, C. *et al.* Inflamed and non-inflamed classes of HCC: a revised
999 immunogenomic classification. *Gut* gutjnl-2021-325918 (2022) doi:10.1136/gutjnl-2021-
1000 325918.
1001 24. Leslie, J. *et al.* CXCR2 inhibition enables NASH-HCC immunotherapy. *Gut* gutjnl-
1002 2021-326259 (2022) doi:10.1136/gutjnl-2021-326259.
1003 25. Marsee, A. *et al.* Building consensus on definition and nomenclature of hepatic,
1004 pancreatic, and biliary organoids. *Cell Stem Cell* **28**, 816–832 (2021).
1005 26. Broutier, L. *et al.* Human primary liver cancer–derived organoid cultures for disease
1006 modeling and drug screening. *Nat. Med.* **23**, 1424–1435 (2017).
1007 27. Nuciforo, S. *et al.* Organoid Models of Human Liver Cancers Derived from Tumor
1008 Needle Biopsies. *Cell Rep.* **24**, 1363–1376 (2018).
1009 28. Blasco, M. A. *et al.* Telomere Shortening and Tumor Formation by Mouse Cells
1010 Lacking Telomerase RNA. *Cell* **91**, 25–34 (1997).
1011 29. Seehawer, M. *et al.* Necroptosis microenvironment directs lineage commitment in liver
1012 cancer. *Nature* **562**, 69–75 (2018).
1013 30. Murphy, D. J. *et al.* Distinct Thresholds Govern Myc's Biological Output In Vivo.
1014 *Cancer Cell* **14**, 447–457 (2008).
1015 31. Nault, J.-C. *et al.* Molecular Classification of Hepatocellular Adenoma Associates With
1016 Risk Factors, Bleeding, and Malignant Transformation. *Gastroenterology* **152**, 880-894.e6
1017 (2017).
1018 32. Zehir, A. *et al.* Mutational landscape of metastatic cancer revealed from prospective
1019 clinical sequencing of 10,000 patients. *Nat. Med.* **23**, 703–713 (2017).
1020 33. Llovet, J. M. & Hernandez-Gea, V. Hepatocellular Carcinoma: Reasons for Phase III
1021 Failure and Novel Perspectives on Trial Design. *Clin. Cancer Res.* **20**, 2072–2079 (2014).
1022 34. Barone, M., Di Leo, A., Sabbà, C. & Mazzocca, A. The perplexity of targeting genetic
1023 alterations in hepatocellular carcinoma. *Med. Oncol.* **37**, 67 (2020).
1024 35. Sampaziotis, F. *et al.* Cholangiocyte organoids can repair bile ducts after
1025 transplantation in the human liver. *Science* **371**, 839–846 (2021).
1026 36. Dijkstra, K. K. *et al.* Generation of Tumor-Reactive T Cells by Co-culture of Peripheral
1027 Blood Lymphocytes and Tumor Organoids. *Cell* **174**, 1586-1598.e12 (2018).
1028 37. Artegiani, B. *et al.* Fast and efficient generation of knock-in human organoids using
1029 homology-independent CRISPR–Cas9 precision genome editing. *Nat. Cell Biol.* **22**, 321–
1030 331 (2020).

38. Xue, R. *et al.* Variable Intra-Tumor Genomic Heterogeneity of Multiple Lesions in Patients With Hepatocellular Carcinoma. *Gastroenterology* **150**, 998–1008 (2016).
39. Percie du Sert, N. *et al.* The ARRIVE guidelines 2.0: Updated guidelines for reporting animal research. *PLOS Biol.* **18**, e3000410 (2020).
40. Madisen, L. *et al.* A robust and high-throughput Cre reporting and characterization system for the whole mouse brain. *Nat. Neurosci.* **13**, 133–140 (2010).
41. Harada, N. *et al.* Intestinal polyposis in mice with a dominant stable mutation of the beta-catenin gene. *EMBO J.* **18**, 5931–5942 (1999).
42. Kruspig, B. *et al.* The ERBB network facilitates KRAS-driven lung tumorigenesis. *Sci. Transl. Med.* **10**, eaao2565 (2018).
43. Marino, S., Vooijs, M., van Der Gulden, H., Jonkers, J. & Berns, A. Induction of medulloblastomas in p53-null mutant mice by somatic inactivation of Rb in the external granular layer cells of the cerebellum. *Genes Dev.* **14**, 994–1004 (2000).
44. Olive, K. P. *et al.* Mutant p53 gain of function in two mouse models of Li-Fraumeni syndrome. *Cell* **119**, 847–860 (2004).
45. Krimpenfort, P., Quon, K. C., Mooi, W. J., Loonstra, A. & Berns, A. Loss of p16Ink4a confers susceptibility to metastatic melanoma in mice. *Nature* **413**, 83–86 (2001).
46. Suzuki, A. *et al.* T cell-specific loss of Pten leads to defects in central and peripheral tolerance. *Immunity* **14**, 523–534 (2001).
47. Murtaugh, L. C., Stanger, B. Z., Kwan, K. M. & Melton, D. A. Notch signaling controls multiple steps of pancreatic differentiation. *Proc. Natl. Acad. Sci. U. S. A.* **100**, 14920–14925 (2003).
48. Jackson, E. L. *et al.* Analysis of lung tumor initiation and progression using conditional expression of oncogenic K-ras. *Genes Dev.* **15**, 3243–3248 (2001).
49. Deng, C., Zhang, P., Harper, J. W., Elledge, S. J. & Leder, P. Mice lacking p21CIP1/WAF1 undergo normal development, but are defective in G1 checkpoint control. *Cell* **82**, 675–684 (1995).
50. Feng, G. J. *et al.* Conditional disruption of Axin1 leads to development of liver tumors in mice. *Gastroenterology* **143**, 1650–1659 (2012).
51. Tsuchida, T. *et al.* A simple diet- and chemical-induced murine NASH model with rapid progression of steatohepatitis, fibrosis and liver cancer. *J. Hepatol.* **69**, 385–395 (2018).

52. Fujii, M. *et al.* A murine model for non-alcoholic steatohepatitis showing evidence of association between diabetes and hepatocellular carcinoma. *Med. Mol. Morphol.* **46**, 141–152 (2013).
53. Chen, S., Zhou, Y., Chen, Y. & Gu, J. fastp: an ultra-fast all-in-one FASTQ preprocessor. *Bioinformatics* **34**, i884–i890 (2018).
54. Ewels, P., Magnusson, M., Lundin, S. & Käller, M. MultiQC: summarize analysis results for multiple tools and samples in a single report. *Bioinformatics* **32**, 3047–3048 (2016).
55. Wingett, S. W. & Andrews, S. FastQ Screen: A tool for multi-genome mapping and quality control. *F1000Research* **7**, 1338 (2018).
56. Yates, A. D. *et al.* Ensembl 2020. *Nucleic Acids Res.* gkz966 (2019) doi:10.1093/nar/gkz966.
57. Dobin, A. *et al.* STAR: ultrafast universal RNA-seq aligner. *Bioinformatics* **29**, 15–21 (2013).
58. Liao, Y., Smyth, G. K. & Shi, W. featureCounts: an efficient general purpose program for assigning sequence reads to genomic features. *Bioinformatics* **30**, 923–930 (2014).
59. Morgan, M. T. & Davis, S. R. GenomicDataCommons: *a Bioconductor Interface to the NCI Genomic Data Commons*. http://biorxiv.org/lookup/doi/10.1101/117200 (2017) doi:10.1101/117200.
60. Mayakonda, A., Lin, D.-C., Assenov, Y., Plass, C. & Koeffler, H. P. Maftools: efficient and comprehensive analysis of somatic variants in cancer. *Genome Res.* **28**, 1747–1756 (2018).
61. Love, M. I., Huber, W. & Anders, S. Moderated estimation of fold change and dispersion for RNA-seq data with DESeq2. *Genome Biol.* **15**, 550 (2014).
62. Durinck, S., Spellman, P. T., Birney, E. & Huber, W. Mapping identifiers for the integration of genomic datasets with the R/Bioconductor package biomaRt. *Nat. Protoc.* **4**, 1184–1191 (2009).
63. Durinck, S. *et al.* BioMart and Bioconductor: a powerful link between biological databases and microarray data analysis. *Bioinformatics* **21**, 3439–3440 (2005).
64. Csardi, Gabor, N., Tamas. The igraph software package for complex network research. *InterJournal* **Complex Systems**, 1695 (2006).
65. Mercatelli, Daniele, G., Federico M. Correlation Tool (CorTo): a simple R package to infer correlation networks using Data Processing Inequality (DPI). (2020).

66. Subramanian, A. *et al.* Gene set enrichment analysis: A knowledge-based approach for interpreting genome-wide expression profiles. *Proc. Natl. Acad. Sci.* **102**, 15545–15550 (2005).
67. Liberzon, A. *et al.* The Molecular Signatures Database Hallmark Gene Set Collection. *Cell Syst.* **1**, 417–425 (2015).
68. Jiménez-Sánchez, A., Cast, O. & Miller, M. L. Comprehensive Benchmarking and Integration of Tumor Microenvironment Cell Estimation Methods. *Cancer Res.* **79**, 6238–6246 (2019).
69. Gu, Z., Eils, R. & Schlesner, M. Complex heatmaps reveal patterns and correlations in multidimensional genomic data. *Bioinformatics* **32**, 2847–2849 (2016).
70. Wickham, H. *ggplot2*. (Springer New York, 2009). doi:10.1007/978-0-387-98141-3.
71. Garnier, S. *et al. sjmgarnier/viridis: viridis 0.6.0 (pre-CRAN release)*. (Zenodo, 2021). doi:10.5281/ZENODO.4679424.
72. Yu, G., Wang, L.-G., Han, Y. & He, Q.-Y. clusterProfiler: an R Package for Comparing Biological Themes Among Gene Clusters. *OMICS J. Integr. Biol.* **16**, 284–287 (2012).
73. Broutier, L. *et al.* Culture and establishment of self-renewing human and mouse adult liver and pancreas 3D organoids and their genetic manipulation. *Nat. Protoc.* **11**, 1724–1743 (2016).
74. de Chaumont, F. *et al.* Icy: an open bioimage informatics platform for extended reproducible research. *Nat. Methods* **9**, 690–696 (2012).

Acknowledgements

We thank the CRUK Beatson Institute's Core Facilities, and in particular Biological Services, Histological Services, Molecular Technology Services, Beatson Advanced Imaging Resource, Bioinformatics, and Central Services for their help. We thank Heather McKinnon for help with drug dosage studies, and Dimitris Athineos for support with animal work. We thank Victoria Min-Yi Wang and Chiara Braconi for discussion and comments on the manuscript. We thank Catherine Winchester for advice with Research Integrity and manuscript editing.

The results shown here are in part based upon data generated by the TCGA Research Network: https://www.cancer.gov/tcga.

Author Contributions

M.Mü contributed to the conceptualization of the project, designed and performed experiments, supervised experiments, analysed data, created the figures and wrote the manuscript (original

draft and subsequent editing). S.M designed and performed in vivo experiments and analysed data. H.H. performed the computational analysis of the disease positioning and created figures. T.J.K. provided histopathological analysis and advice. L.M. contributed to design of mouse HCCO HTP experiments and performed and analysed mouse HCCO HTP experiments under L.M.C. supervision. L.B. and S.N. designed, performed and analysed experiments for human HCCO experiments under M.H.H supervision. T.J. designed and performed in vivo DEN/ALIOS and MWD experiments under O.J.S. supervision. N.P. and S.D. designed and performed in vivo STZ experiments under K.B. supervision. J.L. designed and performed in vivo orthotopic transplant experiments under D.A.M. supervision. J.S. performed experiments and analysed data under T.G.B. supervision. G.M., A.M., and E.J. performed in vivo imaging. M.Mc. and H.L.R. provided resources and useful discussion. J.H. analysed mouse HCCO data. C.K. and A.G. performed in vivo experiments under M.Mü. and T.G.B. supervision. C.N. and W.C. performed experiments. R.S., M.N., and A.H. performed computational analysis. T.D. and E.T. assisted with in vivo experiments under M.Mü. and T.G.B. supervision. D.J.M. contributed resources and useful discussion. D.L. contributed advice and resources. D.A.M., K.B, M.H.H., L.M.C., and O.J.S. contributed useful discussion and provided resources. C.M. supervised computation analysis, contributed useful discussion and provided resources. T.G.B. contributed to the conceptualization of the project, designed and assisted with experiments, supervised, edited the manuscript, and acquired funding. All authors have approved the final version.

Funding

M.Mü. and T.G.B. were funded by the Wellcome Trust (Grant number: WT107492Z) and T.G.B and E.H.T. by the CRUK HUNTER Accelerator Award (Grant number: 175 A26813). S.D, N.P., and K.B. were funded by CRUK (Grant numbers A29799, A17196, and A31287). H.L.R and M.Mc were funded by CRUK centre grant (C9380/A18084), programme grant (C18342/A23390) and Accelerator award (C9380/A26813). C.K was funded by CRUK (Grant number A17196 and A31287). D.L. was funded by Cancer Research UK (Grant number: A25006). L.M.C was funded by Cancer Research UK (Grant number: A23983). O.J.S. was funded by Cancer Research UK (Grant number: A21139, A17196, and A31287). H.H. and C.M. were funded by Cancer Research UK (Grant number: A29801)

Conflict of interest:

Material for the lenvatinib day 15 and day 30 time point experiments (Fig4h-j) was provided by Eisai.

D.A.M. is a Director, shareholder and employee of FibroFind Ltd.

Supplementary Information is available for this paper.

Correspondence and requests for materials should be addressed to m.mueller@beatson.gla.ac.uk. and t.bird@beatson.gla.ac.uk

Supplementary Files

This is a list of supplementary files associated with this preprint. Click to download.

- ExtendedDataTable1.xlsx
- ExtendedDataTable3.xlsx
- SupFigure2.pdf
- ExtendedDataTable2.xlsx
- SupFigure10.pdf
- SupFigure4.pdf
- SupFigure9.pdf
- SupFigure1.pdf
- SupFigure7.pdf
- SupFigure6.pdf
- SupFigure3.pdf
- SupFigure5.pdf
- SupFigure8.pdf